Nanoscale

Nanostructured CeO_2 photocatalysts: Optimizing surface chemistry, morphology, and visible-light absorption

Journal:	*Nanoscale*
Manuscript ID	NR-REV-02-2024-000676.R1
Article Type:	Review Article
Date Submitted by the Author:	19-Apr-2024
Complete List of Authors:	Herzog, Austin; NRC Postdoctoral Associate, US Naval Research Laboratory Michael, Tara; NRC Postdoctoral Associate, US Naval Research Laboratory Dunkelberger, Adam; U.S. Naval Research Laboratory, Chemistry Division (Code 6100) Johannes, Michelle; Naval Research Laboratory, Rolison, Debra; Naval Research Laboratory, Code 6170 DeSario, Paul; US Naval Research Laboratory, Surface Chemistry Branch Novak, Travis; U.S. Naval Research Laboratory

Review

Nanostructured CeO_2 photocatalysts: Optimizing surface chemistry, morphology, and visible-light absorption

Received 00th January 20xx,
Accepted 00th January 20xx

DOI: 10.1039/x0xx00000x

Austin E. Herzog,[a] Tara J. Michael,[a] Adam D. Dunkelburger,[b] Michelle D. Johannes,[c] Debra R. Rolison,[b] Paul A. DeSario,[d] Travis G. Novak[b]*

Emerging photocatalytic applications of cerium dioxide (CeO_2) include green hydrogen production, CO_2 conversion to fuels, and environmental remediation of various toxic molecules. These applications leverage the oxygen storage capacity and tunable surface chemistry of CeO_2 to photocatalyze the chosen reaction, but many open questions remain regarding the fundamental physics of photocatalysis over CeO_2. The commonly ascribed 'bandgap' of CeO_2 (~3.1 eV) differs fundamentally from other photocatalytic oxides such as TiO_2; UV light excites an electron from the CeO_2 valence band into a *4f* state, generating a polaron as the lattice distorts around the localized charge. Researchers often disregard the distinction between the *4f* state and a traditional, delocalized conduction band, resulting in ambiguity regarding mechanisms of charge transfer and visible-light absorption. This review summarizes modern literature regarding CeO_2 photocatalysis and discusses commonly reported photocatalytic reactions and visible light–sensitization strategies. We detail the often misunderstood fundamental physics of CeO_2 photocatalysis and supplement previous work with original computational insights. The exceptional progress and remaining challenges of CeO_2-based photocatalysts are highlighted, along with suggestions for further research directions based on the observed gaps in current understanding.

Introduction

Ceria (CeO_2) offers effective activity for a wide variety of thermo-, electro-, and photo-catalytic reactions. Despite being a 'rare earth' element, cerium is not particularly rare or expensive. It is the most common lanthanide in earth's crust, with abundance similar to many common transition metals (Cu, Ni, Zn)[1] and a 2020 market price of less than 5 USD per kg.

CeO_2 crystallizes in a fluorite structure (space group $Fm\bar{3}m$), with each Ce coordinated by eight O atoms in stoichiometric CeO_2. Most ceria, however, is not perfectly stoichiometric, forming oxygen vacancies (O_{vac}) either on the surface or in the bulk material. Each O_{vac} results in two Ce^{3+} sites (Fig. 1), enabling Ce to easily cycle between stoichiometric (4+) and oxygen-deficient (3+) states to catalyze oxidation reactions. The oxidation of the target molecule by a lattice oxygen and healing of the subsequent O_{vac} by O_2 or H_2O is known as the Mars–van Krevelen (MvK) mechanism. A major thrust of research into CeO_2-based catalysts relies on controlling the O_{vac} concentration, which is impacted by nanoparticle size,[2] exposed crystal facet,[3] or heteroatom doping with trivalent atoms that substitute in Ce sites, such as Gd,[4] Y,[5] La,[6] etc. These persistent O_{vac} sites imposed by dopants can aid catalysis by acting as adsorption and activation sites for O_2 or H_2O.

Nanostructures of CeO_2 can be further optimized for catalysis through preferential exposure of certain crystal planes. The concentration and oxygen mobility of O_{vac} vary significantly depending on which planes are exposed,[7] in some cases even alternating the dominant reaction mechanism (MvK vs. Langmuir–Hinshelwood) by which catalysis proceeds.[8] The Lewis acidity of CeO_2 facets follows the order of: $\langle 111\rangle > \langle 110\rangle > \langle 100\rangle$.[9] Surface hydroxyl concentration can be strongly affected by the exposed facet as well.[10, 11]

These favorable properties, along with the optical aspects discussed in the following section, make CeO_2 an emerging target of photocatalytic research. Many recent reviews on CeO_2 photocatalysts focus on a specific type of reaction, such as energy conversion,[12] environmental catalysis,[13] or degradation of organic pollutants,[14] with minimal discussion of the fundamental physics involved. Indeed, CeO_2 photocatalysis is an active research area with reports of new advances after morphological changes to the CeO_2 structure, and doping with metal and non-metal atoms. These advances would be deepened by a better understanding of the rich photochemistry we outline below.[15-17] In this review, we summarize recent developments of CeO_2-based photocatalysts, clarify fundamental optical properties, provide fresh computational insights, and review common reactions studied. We will also discuss the extensive efforts in sensitizing CeO_2 to visible light through morphological modifications, doping, or plasmonic sensitization, aiming to identify trends across many application spaces.

---

[a] *NRC Postdoctoral Associate, U.S. Naval Research Laboratory, Washington, D.C., 20375, USA*
[b] *Chemistry Division (Code 6100), U.S. Naval Research Laboratory, Washington, D.C., 20375, USA*
[c] *Materials Science and Technology Division (Code 6300), U.S. Naval Research Laboratory, Washington, D.C., 20375, USA*
[d] *Former NRL staff scientist in Code 6100. Current affiliation: Advanced Naval Platforms Division, Office of Naval Research, Arlington, VA, 22203, USA*
E-mail: travis.g.novak.civ@us.navy.mil

Electronic Supplementary Information (ESI) available: [details of any supplementary information available should be included here]. See DOI: 10.1039/x0xx00000x

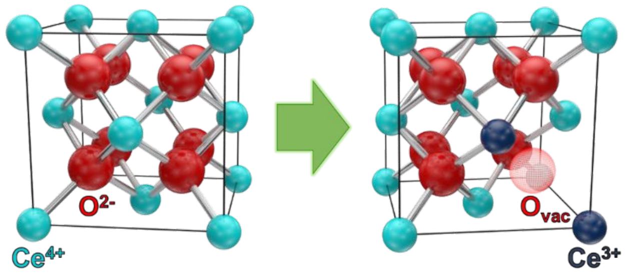

Fig. 1 Illustration of the crystal structure of stoichiometric CeO_2 (left) vs. CeO_2 with an oxygen vacancy (O_{vac}) and two charge-compensating Ce^{3+} sites.

Optical Properties of CeO_2

Before reviewing the photocatalytic activity of CeO_2, we first discuss the optical properties of nanoscale CeO_2 and the electronic energy levels that dictate those optical properties. We draw special attention to critical differences between CeO_2 and the canonical photocatalyst TiO_2 and highlight a few recent experiments interrogating the ultrafast dynamics of the electronic excited states of CeO_2. For a traditional semiconductor, the bandgap is the energy separating the valence band (VB) maximum, which is filled with electrons, to the conduction band (CB) minimum, which is empty. Unlike metals, which retain their electronic band structure down to 3 nm, semiconductors such as TiO_2 and CeO_2, have size- and shape-dependent optical properties that can arise from quantum confinement effects when reduced to the nanoscale (<100 nm).[18, 19] The bandgap energy separating the VB and CB is indirectly related to the size of the nanoparticle, and can be estimated using Eq. 1, where $\boldsymbol{E_g}$ is the bandgap energy of the bulk, $\boldsymbol{m_e}$ is the effective mass of the electron, $\boldsymbol{m_h}$ is the effective mass of the hole, and $\boldsymbol{\varepsilon}$ is relative dielectric constant:[20-22]

$$E = E_g + \frac{h^2}{8R^2}\left[\frac{1}{m_e} + \frac{1}{m_h}\right] - \frac{1.8e^2}{4\pi\varepsilon\varepsilon_0 R} \qquad \text{(Eq. 1)}$$

The bandgap energy for nanoparticles is, in general, blue-shifted relative to the bulk value. When the radius R of the nanoparticle is very small, $1/(R^2)$ dominates and the bandgap energy increases. For traditional semiconductors, therefore, the bandgap can be tuned by adjusting preparation conditions that control the size of the nanoparticles. Controlling the bandgap of CeO_2 is somewhat less straightforward because the definition of the bandgap itself is less straightforward. For TiO_2, the bulk bandgap energy of 3.2 eV (Fig. 2) represents the energy required for a charge-transfer transition from filled *2p* orbitals in O to empty *3d* orbitals in Ti.[19] The electrons promoted to the conduction band are truly free carriers, as is readily shown by their Drude-like free carrier absorption and relatively high mobility. At similar energies in CeO_2, charge transfer takes place from the filled valence band in *2p* orbitals of O to empty *4f* orbitals in Ce.[23] This transition is typically the one described as the “bandgap” for CeO_2 in the literature, but the *4f* level is much more localized than a typical conduction band. The degree of localization of the *4f* level and the manner in which the localization depends on the specific composition and preparation of the CeO_2 is still a topic of active research, but it appears that excitation to this level is responsible for the photocatalytic activity of ceria. Nanostructuring is essential with highly localized carriers to ensure that an interface is within a limited number of hops.

The presence of this *4f* level strongly correlates with the presence of Ce^{3+}. Populating the *4f* level is implicated as a mechanism for interconversion between Ce^{4+} and Ce^{3+} giving rise to mechanisms for charge transport under near-UV excitation even though the true conduction band is 6 eV above the valence band.[23, 24] Despite the clear differences between this *4f* level and a “true” CB such as that accessible in TiO_2, we will adopt the predominant language of the literature and refer to this transition energy as the bandgap in the discussion that follows.

A wealth of literature describes numerous strategies that effectively tune the bandgap of CeO_2, with two prevailing and sometimes overlapping schools of thought regarding the mechanism of tuning. One proposed mechanism is quantum confinement explained above and dictated by Eq. 1, targeting the nanoparticle size as the key parameter. The size, and thus the bandgap, can be altered intrinsically through nanostructuring strategies and extrinsically through lattice substitution, i.e., doping. Doping can reduce the bandgap of semiconductors by altering the lattice structure, and therefore the optical properties. The second proposed mechanism is independent of particle size and relies on electronic transitions of the constituent atoms of the nanoparticles. Because changing constituent atoms often changes the particle radius for otherwise similar preparation techniques, the two mechanisms can be difficult to differentiate. In the course of briefly reviewing reports of bandgap tuning in ceria below, we will point out the mechanism identified by the authors.

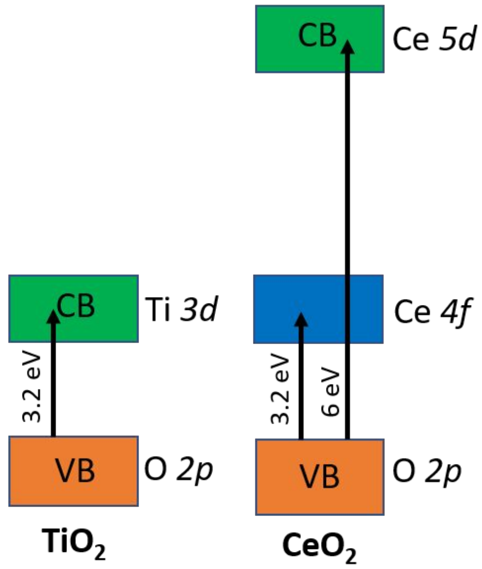

Fig. 2 Energy-band diagram of TiO_2 and CeO_2.

Lin and coworkers synthesized CeO_2 nanocrystals doped and undoped with lanthanide ions (Eu^{3+}, Tb^{3+}, Sm^{3+}).[25] The undoped CeO_2 shows strong absorption below 400 nm due to the *2p* (O^{2-}) to *4f* (Ce^{4+}) transition (see Fig. 3A). The doped CeO_2:Eu^{3+} shows a red shift in the maximum absorption and increased absorption near 500 nm due to the replacement of Ce^{3+} with Eu^{3+} on the surface. This red-shift is caused by the larger atomic radius of Eu^{3+} compared to the more stable and smaller Ce^{4+} found in undoped CeO_2.[25]

Blondeau and coworkers, on the other hand, report a blue-shift in absorption of CeO_2 when doping CeO_2 nanostructures with Ca^{2+} concentrations ranging from 0–50 mol%.[21] Below 20 mol% doping, the samples are single phase CeO_2 in the cubic fluorite structure. At concentrations of 30 mol% and above, a layer forms in which Ca^{2+} ions replace Ce^{4+}. The pure CeO_2 sample shows strong absorption near 315 nm, while the samples doped with Ca^{2+} show strong absorption closer to 300 nm due to a smaller atomic radius (Fig. 3B). Studies regarding doping of CeO_2 for photocatalytic applications are discussed further in a later section.

The experimental bandgap can be obtained using a Tauc plot shown in Eq. 2 where $h\nu$ is the photon energy, α is the absorption coefficient, and the intersection of the extrapolated linear portions gives the direct bandgap energy when x = 2, and the indirect bandgap energy when x = ½.

$$(\alpha h\nu)^x \; vs \; h\nu \qquad \text{(Eq. 2)}$$

Fig. 3C and 3D show the Tauc plots for nanostructured CeO_2 and CeO_2 doped with 30 mol% Ca^{2+}. The intercepted linear portions give an experimental direct bandgap energy of 3.2 eV for the nanostructured CeO_2 and 3.46 eV for CeO_2 doped with 30 mol% Ca^{2+}. We caution that the use of Tauc plots for CeO_2 may be somewhat misleading due to the localized character of the *4f* state. Tauc plots are limited in cases where mid-gap defects dominate optical absorption or bands are not parabolically shaped.[26] Direct comparisons to transitions to delocalized conduction bands brush over the rich physics of CeO_2.

Samiee and Goharshadi base precipitated cerium oxide using either Ce(III) or Ce(IV) salt precursors.[22] Using a Ce(III) precursor (cerium nitrate) requires an additional oxidation step, resulting in larger particle sizes (d = 7.2 nm). Using Ce(IV) precursors (cerium ammonium nitrate or cerium sulfate) yields smaller particle sizes (d = ~5 nm), resulting in larger blue-shifts in bandgap energy (Table 1).

Recent work by Mayer and coworkers summarizes the case for the size-independent mechanism, finding that the ratio of Ce^{3+} to Ce^{4+} correlates with the near-UV absorption spectrum of nanoscale ceria, corroborating the importance of species-specific electronic transitions.[27] Using a suite of in situ reduction and oxidation chemistries, they showed that the overall intensity of the bandgap transition is directly linear to the proportion of Ce^{3+} in ceria nanoparticles. With a higher concentration of Ce^{3+}, the absorption intensity decreases and the absorption band appears to blue-shift, as would be expected for smaller particles. Critically, the size of the particles remains constant over the course of the redox reactions; quantum confinement, therefore, is not responsible for the changing optical properties.

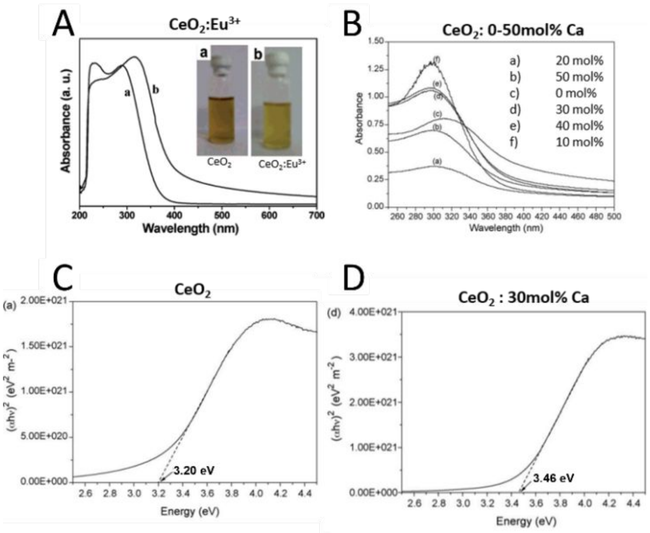

Fig. 3 UV–Vis absorption of CeO_2 doped with and without (A) Eu^{3+} and (B) Ca^{2+}. The absorption curves in (B) were used to create Tauc plots such as those seen in (C) and (D). Reprinted with permission from Ref. 15 Copyright 2010, Elsevier.

The differences between the electronic structure of CeO_2 and more traditional semiconductors leads to key conceptual differences in the time-resolved spectroscopy of ceria. Time-resolved spectroscopy has been used extensively to elucidate the mechanisms of electron transport in photocatalytic systems such as TiO_2, but only recently have groups started to explore the dynamics of ceria. Pioneering work by Cresi et al. employed ultrafast transient absorption spectroscopy on a 6 nm thin film of CeO_2 to definitively show that when electrons enter the *4f* level in ceria, the electrons polarize a portion of the lattice structure to form a polaron.[28] Fig. 4A shows a schematic of the localized lattice distortion in the presence of a free electron that forms a potential well, increasing the effective mass of the electron and decreasing its mobility. Upon excitation with 275 nm light, the VB to *4f* transition photobleaches (PB) coincident with photoinduced absorption (PIA) from the *4f* to *5d* conduction band (Fig. 4B).[28] This photoinduced absorption is an elegant demonstration of the critical difference between ceria and titania discussed above, namely the so-called bandgap transition occurs to the *4f* state. The formation of the polaron stabilizes the *4f* level relative to the conduction band, and so the absorption maximum shifts from ~3.44 eV at 0.2 ps to ~3.55 eV at 2 ps.

Very recently, the Meyer and Cresi groups independently reported on the dynamics of nanoscale CeO_2 sensitized with nanostructured gold. Spurio et al. use thin-film ceria deposited on an array of gold nanoparticles[29] while Ghosh et al. use gold-ceria core–shell nanoparticles.[30] In either case, exciting the gold nanoparticles with visible light populates the ceria *4f* band, but with no evidence of promotion to the conduction band. As shown by Ghosh et al., photocatalytic behavior is still readily observed; conduction band electrons are not required to drive chemistry.

Table 1. Maximum absorption wavelength from UV–Vis absorption data, estimated bandgap energy from Tauc plot, and optical particle size of nanoceria samples.

Precursor	$\lambda_{max,\,UV}$ **(nm)**	E_g **(eV)**	***d*** **(nm)**
Cerium Nitrate	317	3.48	7.2

Cerium Ammonium Nitrate	225	5.16	5.1
Cerium Sulfate	221	5.33	4.9

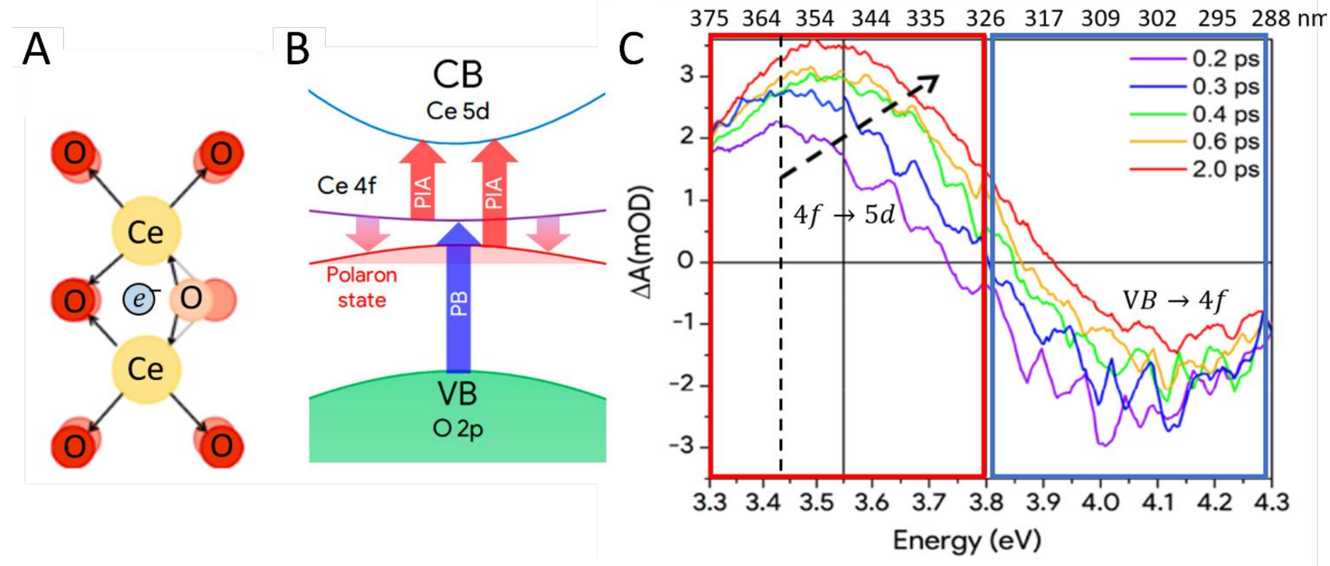

Fig. 4 (A) Schematic of polaron formation in CeO_2. (B) Energy diagram showing photobleaching from the valence band to the Ce *4f* state and photoinduced absorption from the Ce *4f* to *5d* state. (C) Ultrafast transient absorption measurement of the photobleaching and photoinduced absorption of a thin film of CeO_2 following 275 nm excitation. Reprinted with permission from Ref. 28, Copyright 2020, American Chemical Society.

Synthesis of CeO_2

CeO_2 nanostructures are synthesized through many solution-phase routes, where tuning the precursors, reaction temperature, or reaction time influences the morphology of the resulting particles. Alternatively, CeO_2 can be grown through vapor-phase techniques over nanostructures or synthesized through thermal decomposition of appropriate salts.

A common technique for simple, scalable synthesis of CeO_2 nanoparticles is the precipitation method, where a Ce salt (most commonly cerium nitrate) along with any desired metallic dopants are dissolved in solution and titrated until a precipitate can be isolated.[31] Surfactants such as polyvinyl pyrrolidone (PVP) or cetyltrimethylammonium bromide (CTAB) promote smaller crystallite sizes,[32] while non-metallic dopants, such as N or S, can be incorporated into CeO_2 through addition of appropriately soluble molecules.[33, 34] If metallic nanoparticles are present in solution, CeO_2 is seeded onto the surface during titration to form core-shell structures.[35, 36] The precipitate is typically isolated through centrifugation or filtration and calcined at the desired temperature to promote crystallinity. Alternatively, cerium nitrate can simply be thermally decomposed to deposit CeO_2 nanoparticles (NPs) onto existing nanostructures,[37] or dissolved in solution and electrodeposited onto a target substrate.[38]

Hydrothermal methods are closely related to precipitation methods, involving a similar slurry of Ce salts and titrating agents, but take place in aqueous solutions at elevated temperature and pressure in a sealed autoclave. Hydrothermal methods offer additional avenues for optimization, as adjustments to the pressure and temperate further refine morphology. When synthesis takes place in the presence of organic solvents instead of or in addition to water, it is dubbed a 'solvothermal' method.[39] Many studies leverage multiple solution phase techniques to directly compare the performance of different CeO_2 nanostructures, as shown in the production of CeO_2 nanoflakes (NF-CeO_2) through a co-precipitation method and CeO_2 nanorods (NR-CeO_2) through a hydrothermal method (Fig. 5).[40]

Another type of solution-phase synthesis is the sol–gel method, where a colloidal suspension of particles undergoes a hydrolysis reaction to form metal–oxygen–metal bonds. Eventually these particles grow and condense to form a 3D, porous network of nanoparticles with liquid trapped in the pores. Capillary forces will usually collapse the structure if left to dry under ambient conditions, resulting in a powder – dubbed a xerogel – that is still relatively high surface area.[41] Alternatively, the wet gel can be supercritically dried to avoid capillary forces and preserve the 3D interconnected network, resulting in an aerogel. Our group currently uses a modified method originally developed by Gash and coworkers,[42] to synthesize CeO_2 and Gd-doped CeO_2 (GCO) aerogels for various catalytic applications.[4, 43, 44]

These solution-phase techniques can be performed in the presence of other materials as a facile way to create photocatalytic composites; examples include adding graphitic carbon nitride powder to a typical hydrothermal CeO_2 batch to create CeO_2/g-C_3N_4,[45] spin-coating CeO_2 sol–gels onto conductive substrates,[46] and co-precipitating CeO_2 onto ZnO NPs.[47] Researchers can also employ sacrificial polymer or silica templates to create mesoporous structures based on these methods.[48, 49]

Most nanostructured CeO_2 photocatalysts are synthesized through solution-phase synthesis methods, but some vapor-phase methods have been studied as well. Atomic layer deposition (ALD) is capable of growing precise layers of CeO_2 on other nanostructures,[50]

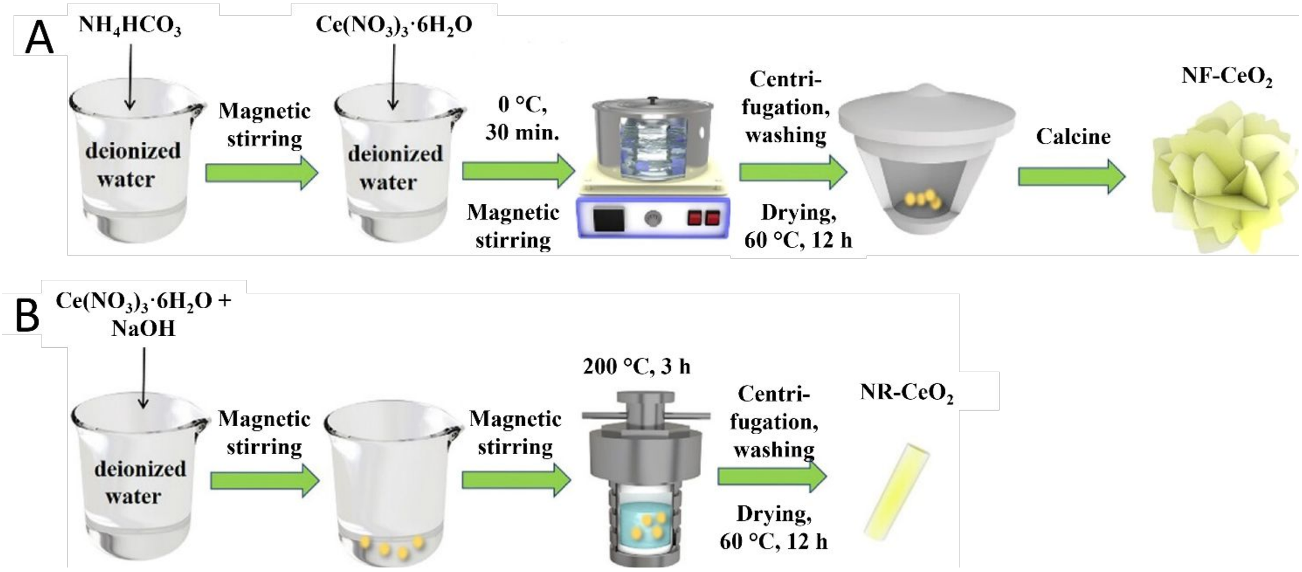

Fig. 5 (A) Co-precipitation method for synthesis of CeO_2 nanoflakes (NF-CeO_2). (B) Hydrothermal method for synthesis of CeO_2 nanorods (NR-CeO_2). Reprinted with permission from Ref. 40, Copyright 2023, American Chemical Society.

albeit at the expense of scalability. Molecular beam epitaxy (MBE) is another thin film deposition technique useful for model studies of CeO_2.[28, 29, 51]

Computational Insights

Experimental estimates of the CeO_2 bandgap, optical gap, spread of *4f* levels, and polaron energies differ quantitatively but agree qualitatively with each other and with first-principles calculations. We use the previously discussed optical study by Cresi et al.[28] as a comparison for our original calculations in the following figures (Fig. 6, 7, 8).

Methodology

Density Functional Theory (DFT) accurately reproduces both structural and electronic properties, provided that the electronic properties of the materials of interest are close enough to the materials that underpin the methodology's central approximation, or a related version: the local density approximation (LDA) or the generalized gradient approximation (GGA). The electron–electron interaction at a given locality can be approximated with the interaction of a uniform electron gas of the same density as that locality. The method works well for well-screened systems (metals) and uncorrelated materials in which specific electron–electron interactions are unimportant.

One predominant error in DFT is underestimation of gaps, sometimes badly enough that insulators end up calculated to be metals. CeO_2 contains extremely localized (unscreened) *4f* states that interact in very non–mean-field ways with each other as well as localized *5d* states. Since both states are necessary to reproduce the band and optical gaps, they must both be treated correctly but are not using either LDA or GGA.[52] A commonly used and often successful correction is the DFT+U approach[53] which adds an ad-hoc parameter "U" to a specific set of atomic orbitals (e.g., *4f* or *5d*). This correction localizes the selected orbitals (compared to LDA or GGA) and also shifts the energy of occupied orbitals downward and unoccupied orbitals upward, thus often bringing the gap into closer agreement with reality. This approach offers a computationally efficient method of dealing with localized states, although a separate "U" must be chosen for each orbital complex of interest and mis-establishing "U" can result in important errors in calculated electronic and structural properties.

Another approach is the so-called hybrid functional approach which treats all orbitals of all atoms on the same footing by mixing in some fraction of exact exchange to the LDA/GGA exchange approximation. This formalism has been remarkably successful in reproducing electronic properties for many correlated/localized systems and is what we use in this work. A mixing fraction and range must be chosen overall, so this method is also ad hoc at some level, but arguably less so than DFT+U. It also comes at a computational cost of approximately an order of magnitude more than LDA/GGA or DFT+U.

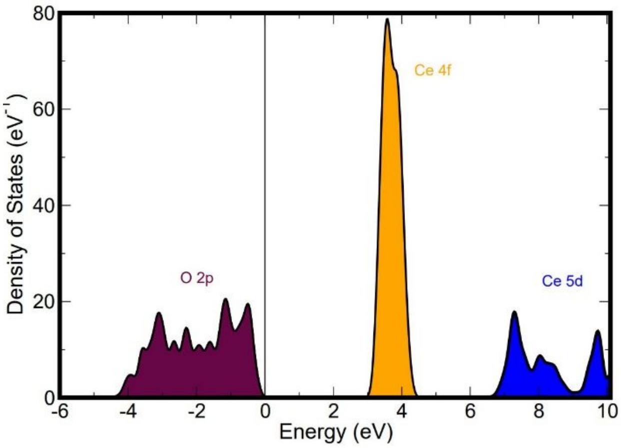

Fig. 6 Density of states of CeO_2 as calculated with the HSE06 functional.

As seen in Fig. 6, our energy complex placements using HSE06 match those of Cresi's fast transient-absorbance spectroscopy (FTAS)[28] extremely well. Castelton et al. report that DFT+U with an optimal value of "U" = 6 eV on the Ce *4f* states brings the hopping barrier into closer agreement with experiments than does HSE06.[54] Unfortunately, due to deficiencies in most commercial DFT codes, a "U" can be applied to either the Ce *4f* states or to the Ce *5d* states, but not to both simultaneously. Thus, the tendency of DFT+U to push unoccupied states upward drives the Ce *4f* states toward the Ce *5d* states, significantly narrowing the distance between them compared to experiment (Fig. 6). As we are mainly interested in the energy positions of the electronic states in CeO$_2$, we rely on HSE06, especially because occupied *4f* states that occur with polaron formation will be treated at the same level of approximation as the rest of the electronic structure. One can argue that occupied and unoccupied *4f* states would require a separate "U" value to be treated accurately in DFT+U.

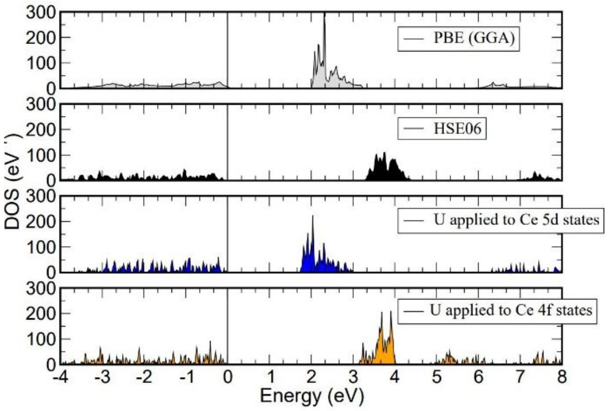

Fig. 7 Comparison of DFT+U vs. HSE06 in terms of band complex placement.

Polaron Formation

Polarons are localized electrons and are substantially different from band electrons. A photoexcited electron in CeO$_2$ is a very good example of a polaron. The electron remains at a specific Ce site, rather than delocalizing into a band, the surrounding negatively charged oxygen ions pull away from the more positive Ce^{3+}. This lattice distortion "traps" the electron such that if it moves to another site, the oxygens at the new site must distort and the oxygens at the old site must return to their equilibrium positions. A polaron is an electron dressed by a phonon, in the language of field theory. The strength of the electron–phonon coupling is what predominantly determines the hopping barrier which, in turn, is the predominant determination of electronic conductivity.

To model a polaron, we add an extra electron to a 3×3×3 supercell of CeO$_2$ and add a uniform background charge spread throughout the cell with an integrated positive charge that exactly compensates the extra electron. We then allow both electronic and ionic systems to relax to the ground state. The results can be seen in Fig. 8. A single Ce *f* state can be seen to split off from the overall Ce *4f* complex and sits at around 3.1 eV. This state carries the full spin of the electron, 1μ_B. In this figure, we shift the energies so that the zero of energy remains at the VB maximum of stoichiometric CeO$_2$ for easier comparison of the various gaps and energy distances. Note that the zero state typically represents the highest occupied state, but that in this case, the polaron state at 3.1 eV is filled. The O *2p* and Ce *5d* complexes remain unchanged from their positions in the stoichiometric case (Fig. 6). In reality, the photoexcited electron would leave a hole in the O *2p* complex, which is difficult to realistically model with DFT, but should not change the overall energy position, although a hole state would appear above the zero-energy line.

We also plot the spin charge density associated with the polaronic state in real space (Fig. 8B). The eight lobes of the charge density do not point along the cardinal axes nor along the Ce–O bond length, identifying the polaron as the f_{xyz} or $f_{z(x2-y2)}$ orbital. The Ce–O bond distance in our calculation of CeO$_2$ is 2.3 Å. The nearest neighbor Ce–O distance around the polaron lengthens to 2.37 Å with the second nearest-neighbor distance shrinking to 2.27 Å. The shorter bonds are imaged in Fig. 8B, as imaging the longer ones would obscure the charge density.

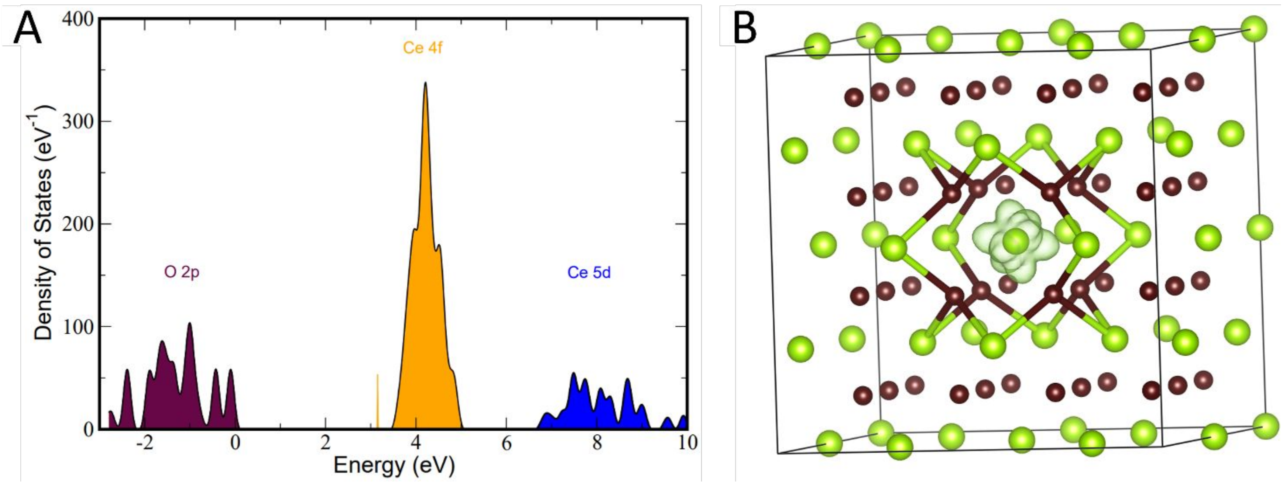

Fig. 8 (A) The density of states of CeO$_2$ with one extra electron that localizes at a Ce site to form a polaron. (B) Image of the spin charge density of the polaron localized on Ce^{3+}; Ce: green; O: brown. The Ce–O nearest-neighbor distance is shortened while next-nearest neighbor distances (imaged) are extended.

We have calculated the polaron hopping barrier using HSE06, as have groups before us, notably Castelton et al.[54] We find an unusually low barrier of less than 10 meV. This energy should be re-evaluated with a more sophisticated method of creating a polaron that accommodates the core–hole in the oxygen states that binds to the polaron, thereby restricting hopping. Oxygen vacancies, which are known to be quite mobile in CeO_2, may hop along with the polaron, further restricting polaron movement from site to site.

Common Reactions Photocatalyzed by CeO_2

Rather than cover every photocatalytic reaction studied over CeO_2, we divide the most common research thrusts into three categories: water-splitting reactions, CO_2 reduction, and environmental remediation or decontamination reactions.

Water-Splitting Reactions

The push for more efficient water-splitting catalysts is driven by a demand for green H_2 – i.e., hydrogen that is produced through electrolysis of water rather than reformed from fossil fuels. The cathodic and anodic sides of this process are the hydrogen evolution reaction (HER) and oxygen evolution reaction (OER), respectively. In cases where only one side of the reaction is to be evaluated, a charge-balancing electron donor (for HER) or electron acceptor (for OER) can be used. Excitation with an appropriate wavelength promotes an electron to the CB and forms a hole in the VB. For the reaction to work, the bottom of the CB must be below the redox potential of H^+/H_2 (–0.41 V vs. NHE at pH = 7) and the top of the VB must be above the redox potential of O_2/H_2O (+0.81 V at pH = 7). In the case of CeO_2, we will refer to the *4f* state as the CB to avoid confusion with numerous works referring to it as such, despite the fundamental differences highlighted earlier. Photocatalysis may take place under electrically neutral conditions or with anodes and cathodes under an applied potential (photoelectrochemical – PEC – water splitting).

For HER, CeO_2 is more commonly used as a supporting oxide complementary to other active components, but nanorods show moderate activity under a simulated solar spectrum using $Na_2S - Na_2SO_3$ as a sacrificial agent.[55] The O_{vac} concentration correlates positively with HER performance, but the rate of the optimized material (5.0 $\mu mol \cdot g^{-1} \cdot h^{-1}$) is still orders of magnitude below the best photocatalytic HER catalysts.

Although it is possible to photocatalyse one or even both sides of the water-splitting reaction using a single material of appropriately wide bandgap, in practice it is difficult to find materials that fulfil all the necessary criteria. An alternative is to use two photocatalytic materials in a heterojunction. For water-splitting applications, these are typically traditional Type-II, where electrons transfer to a lower energy CB edge and holes to the higher energy VB edge, or Z-scheme heterojunctions, where charges transfer between VB and CB (Fig. 9A).[56, 57] A Z-scheme heterojunction can be created with a solution-phase redox mediator (e.g., $Fe^{2+} \rightleftarrows Fe^{3+}$), a solid-state mediator, or without a mediator. In the final case, charges transfer directly between semiconductors: a direct Z-scheme heterojunction.

Photocatalytic water-splitting catalysts have employed CeO_2 to fill various roles in composite materials utilizing these schemes. CdS is a common pairing with CeO_2 for HER, albeit with some debate over the dominant mechanism. Ma et al. assert, based on photoluminescent detection of hydroxyl radical (·OH), that the CdS/CeO_2 junction must act as a Z-scheme, as the radical must originate from the VB of CeO_2 rather than CdS.[58] Wang et al. similarly argue that $Mn_{0.2}Cd_{0.8}S$ and CeO_2 form a direct Z-scheme photocatalyst for HER.[59] In

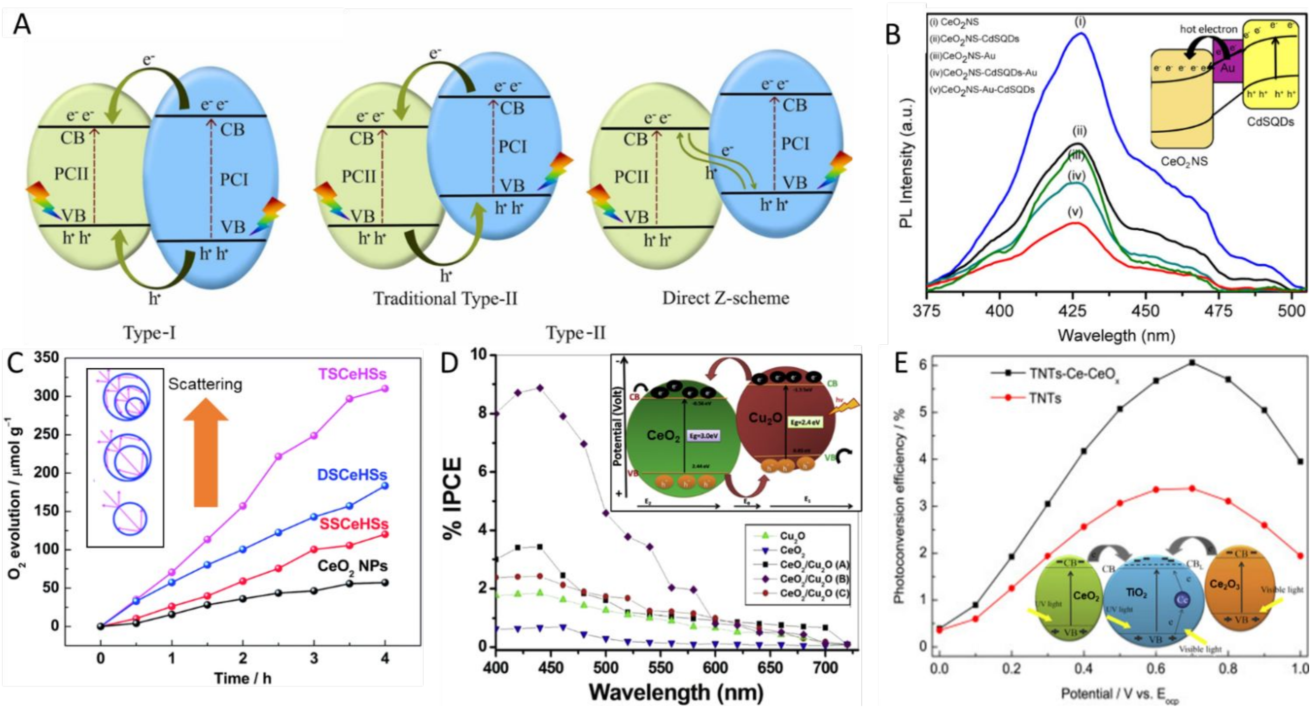

Fig. 9 (A) Illustration of different charge-transport schemes in heterojunctions. Reprinted with permission from Ref. 56, Copyright 2013, American Chemical Society. (B) Quenching of photoluminescence with CdSQDs/Au/CeO_2 (inset: proposed charge-transfer pathways). Reprinted with permission from Ref. 60, Copyright 2017, American Chemical Society. (C) O_2 evolution rate with multi-shelled CeO_2 (inset: increasing internal reflection with shell number). Reprinted with permission from Ref. 68, Copyright 2021, Royal Society of Chemistry. (D) IPCE of Cu_2O/CeO_2 heterojunction as a function of wavelength. Reprinted with permission from Ref. 46, Copyright 2016, Elsevier. (E) Photoconversion efficiency of titanium nanotubes (TNTs) and TNTs in a CeO_2/Ce_2O_3 heterojunction. Reprinted with permission from Ref. 71, Copyright 2016, Elsevier.

T

contrast, Sultana et al. synthesize CeO_2 nanosheets with CdS quantum dots and Au nanoparticles for HER and produce H_2 at a remarkable rate of 12,500 $\mu mol\cdot g^{-1}\cdot h^{-1}$.[60] Both Au and CdS enhance light absorption, while Au promotes hot electron injection into the CeO_2 CB to facilitate HER. A recent study concurs that CdS $\rightarrow CeO_2$ electron transfer is the dominant mechanism (i.e., not a Z-scheme), and finds the photocatalytic activity of preferential $\langle 311 \rangle$ CeO_2 nanorods is significantly higher than that of $\langle 220 \rangle$ CeO_2 nanosheets.[40]

Many other nitrides,[61, 62] oxides,[63-65] or sulfides [39, 61, 66] have been paired with CeO_2 for photocatalytic HER as a means to operate as either Z-scheme or Type-II heterojunctions depending on the band alignment (Table 2). Regardless of where the photoelectron transfers, the result is reduced photoluminescent (PL) recombination upon forming the heterojunction. Fig. 9B shows the effect of promoting charge transfer on PL emission in between CeO_2 nanosheets and CdS quantum dots, with Au facilitating hot electron injection.[60]

CeO_2 is not as frequently studied for the OER side; more commonly studied photocatalysts are based on TiO_2, $BiVO_4$, or WO_3,[67] but Qi et al. demonstrate the potential of multi-shelled CeO_2 using $AgNO_3$ as an electron scavenger, finding greater performance than shells with fewer layers due to increased reflection of incident light and increased surface area, which promotes separation of electron–hole pairs (Fig. 9C).[68] When pH is decreased from 4.3 to 1.0, photogenerated superoxide reacts with H^+ to form H_2O, thereby suppressing OER. When pH is raised to 7.8, Ag^+ ions hydrolyze in a competing reaction.

Many of the materials-design considerations of PEC water-splitting devices are similar to those of pure photocatalysts, with a key difference being that in the PEC setup the half reactions take place at a separate anode and cathode rather than occurring entirely at the material/electrolyte interface. Generally, only one of the electrodes is a photocatalyst (i.e., a photoanode or a photocathode), while the other is a simply an electrocatalyst known to be effective at catalyzing the complementary half reaction (e.g., Pt for HER).

Sharma et al. presented an early study of PEC water splitting using CeO_2/Cu_2O thin films, with a maximum incident photon current efficiency (IPCE) of 1.94% and peak current density of 2.89 mA cm^{-2}.[46] Fig. 9D shows the IPCE as a function of wavelength with a charge-transfer schematic; overall the device performs well at higher incident energies but struggles to harvest lower wavelengths, a common issue with oxide PEC catalysts. The authors assert higher surface roughness and increased defect density improve overall performance.

CeO_2 has also been used in conjunction with various n-type oxides for PEC water-splitting catalysts. Seo et al. employed CeO_2 as a hole-extraction layer with $BiVO_4$ – a well-studied photoanode material – and CoO_x – an OER co-catalyst – finding that the combination greatly outperforms any individual component.[69] The composite achieves a photocurrent of 4.0 mA cm^{-2} and Faradaic efficiency of 91%.

CeO_2 has been employed in hybrids with various ZnO[47, 70] or TiO_2 nanostructures[37, 71, 72] using similar schemes; in all cases the oxide heterojunction aids in charge separation and visible-light harvesting. Work by Tan et al. is notable both for its exceptional performance and unique proposed mechanism of charge transfer.[71] Using an electrochemical method, the authors prepare TiO_2 nanotubes covered with CeO_x – containing stoichiometric CeO_2, Ce_2O_3, and metallic Ce – achieving peak photocurrent and IPCE of 11.2 mA cm^{-2} and 6.1%, respectively. Fig. 9E shows the photoconversion efficiency as a function of applied potential along with an inset schematic showing CeO_2, TiO_2, and Ce_2O_3 band alignments.

CO_2 Reduction

Efforts to capture and utilize carbon emissions have naturally generated increased research attention into catalysts that can turn CO_2 into fuels (CO, CH_4, methanol, etc.), or other useful products. Pure CeO_2 has been studied for CO_2 reduction to methanol, where it was found that O_{vac} concentration promotes methanol yield.[73] Increased O_{vac} concentration by oxalic-acid treatment also promotes CO_2 reduction to CO by capturing photogenerated electrons and thwarting charge recombination.[74]

Another consideration for CeO_2-based CO_2 reduction catalysts is the effect of preferentially exposed facets and their impact on surface chemistry. Zhu et al. compared CeO_2 nanorods – preferentially $\langle 110 \rangle$ – and nanocubes – preferentially $\langle 100 \rangle$ – and found the former significantly more active for CO production.[10] The proposed mechanism requires electron donation from highly electronegative hydroxyls on the CeO_2 surface and electron donation to O_{vac} to form HCO_3^-, followed by reduction of the HCO_3^- to CO_2^- with a photoexcited electron and regeneration of hydroxyls to liberate CO gas (Fig.

Table 2. H_2 evolution rate and proposed charge-transfer schemes for notable CeO_2 HER catalysts

Material	Proposed Charge Transfer	H_2 Evolution Rate (μmol h^{-1} g^{-1})	Ref.
CeO_2	Na_2S – Na_2SO_3 sacrificial agent	5	55
CdS QDs/CeO_2	Direct Z-scheme	101	58
$Mn_{0.2}Cd_{0.8}S$/ CeO_2	Direct Z-scheme	8730	59
CeO_2-Au-CdS	Traditional Type-II	12475	60
CeO_2@Ni_4S_3	Type-II + TEOA sacrificial agent	3740	61
N-CeO_{2-x}/g-C_3N_4-HS	Traditional Type-II	43	62
CeO_2-Fe_2O_3	(not stated)	7184	63
CeO_2/$CeVO_4$/ V_2O_5	Direct Z-scheme	47	64
CeO_2-CuO QDs	Traditional Type-II	2481	65
CeO_2/CZTS	Traditional Type-II	2930	39

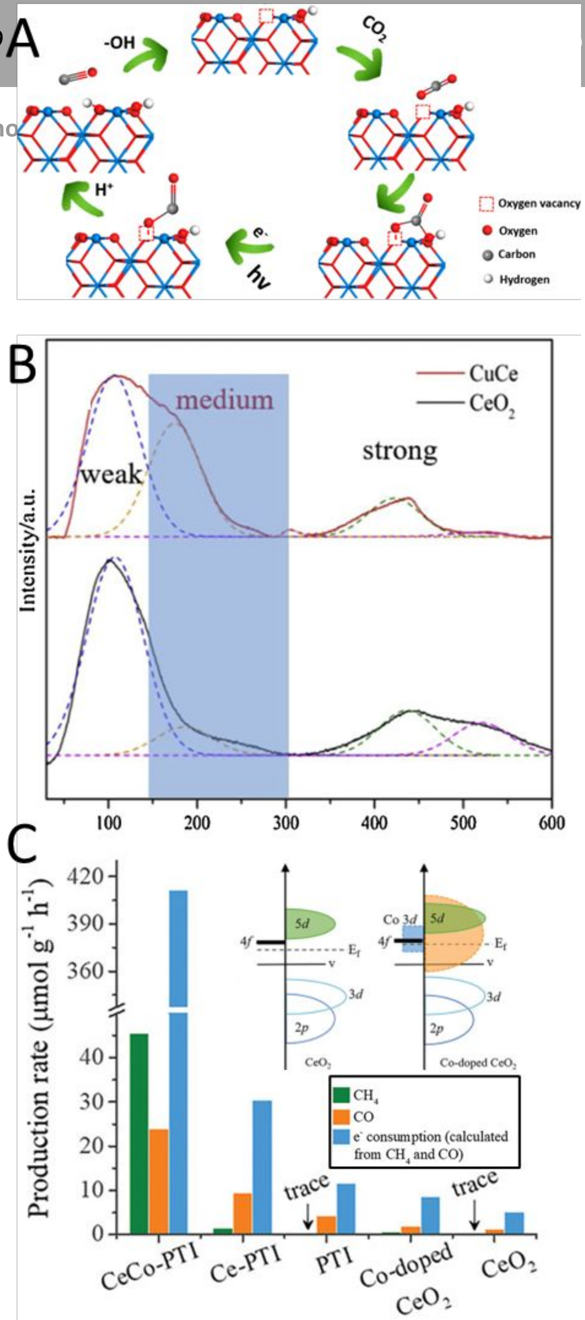

Fig. 10 (A) Proposed mechanism of CO_2 reduction over CeO_2. Reprinted with permission from Ref. 10, Copyright 2020, American Chemical Society. (B) CO_2-TPD showing increase in basic sites with CuCe compared to CeO_2. Reprinted with permission from Ref. 75, Copyright 2019, Elsevier. (C) CO/CH_4 yield and e^- consumption, with inset showing the proposed modification of CeO_2 with Co doping. Adapted with permission from Ref. 79, Copyright 2022, Wiley-VCH.

10A). The higher hydroxyl concentration in preferentially ⟨110⟩ nanorods are deemed responsible for greater CO_2 activation.

Although pure CeO_2 is active for several CO_2 reduction reactions, it is more commonly used in conjunction with other oxides or non-oxide semiconductors to thwart charge recombination and promote balanced reactions, similar to the aspects discussed for water-splitting reactions. Wang et al. demonstrate syngas (CH_4 + CO) production using mesoporous CeO_2/TiO_2 composites under simulated solar illumination, finding that the mesoporous structures greatly outperform commercial Degussa P25.[48] The illumination source used had 'about 50 % visible light', and the authors assert based on Tauc plots that enhanced visible-light absorption is responsible for improved CO and CH_4 yields when CeO_2 is present. The composite also outperforms pure CeO_2 of a similar mesoporous architecture, possibly due to TiO_2 promoting a higher concentration of the Ce^{3+} sites necessary for CO_2 adsorption.

Another oxide composite evaluated by Pu et al. finds that Cu_2O/CeO_2 nanoparticles are effective for reduction of CO_2 to CO.[75] Compared to pristine CeO_2, Cu_2O/CeO_2 increases the number of medium basic sites, as shown in the CO_2 temperature-programmed desorption (TPD) profiles in Fig. 10B. The proposed mechanism is adsorption of CO_2 on Cu sites to form carboxylate (CO_2^-), cleavage of a C–O bond by a photoexcited electron, and transfer of the liberated O to an O_{vac} on the CeO_2 surface. Cu_2O is also employed as a complementary material to CeO_2 in a $Cu_2O/WO_3/CeO_2$ double Z-scheme catalyst for CO_2 reduction to methanol in the presence of DMF, H_2O, and triethylamine (TEA).[76]

Among non-oxide pairings with CeO_2, graphitic carbon nitride (g-C_3N_4) is highly suitable due to its moderate bandgap (2.7 eV) and excellent thermal/chemical stability. Li et al. demonstrate photocatalytic reduction of CO_2 to CO using phosphate-modified CeO_2 with g-C_3N_4.[45] PO_4^{3-} is asserted to enhance Lewis acid sites on the CeO_2 surface for adsorption/activation of CO_2 as well as promote charge transfer from g-C_3N_4 to CeO_2. Other studies on CeO_2+g-C_3N_4 elucidate the beneficial effects of O_{vac} promotion.[77, 78]

A notable recent work by Cheng et al. uses Co-doped CeO_2 with crystalline carbon nitride in an S-scheme photocatalyst for conversion of CO_2 to CH_4.[79] A sub-class of Type-II heterojunction in which exact distinction between an S-scheme and direct Z-scheme photocatalyst can be contentious; common elements of junctions identified as 'S-scheme' include a built-in electric field at the junction and subsequent band bending.[80-82] For Co-doped CeO_2, Co-centered sites draw electrons from carbon nitride due to modification of the electronic structure, increasing both yield and fractional selectivity towards CH_4 (Fig. 10C).[79]

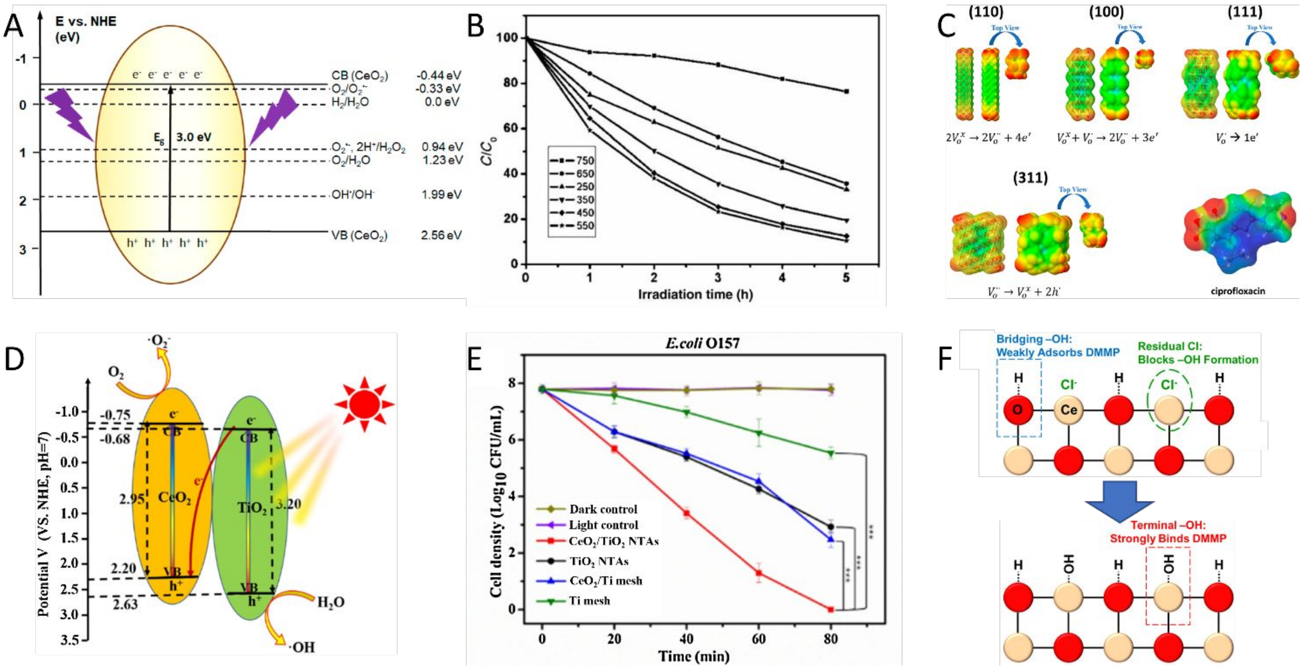

Fig. 11 (A) Band positions of CeO$_2$ in redox potential of common ROS species. Reprinted with permission from Ref. 87, Copyright 2021, Elsevier. (B) Degradation of AO7 with CeO$_2$ calcined at various temperatures. Reprinted with permission from Ref. 90, Copyright 2012, Taylor & Francis. (C) Electron density over various facets of CeO$_2$, along with the target molecule cirproflaxin. Reprinted with permission from Ref. 105, Copyright 2019, American Chemical Society. (D) Proposed mechanism for •OH and •O$_2^-$ formation at CeO$_2$/TiO$_2$ and (E) *E. coli* cell density as a function of time under illumination with various photocatalysts. Reprinted with permission from Ref. 106, Copyright 2021, Elsevier. (F) Illustration of a Cl-fouled vs. terminal –OH rich CeO$_2$ surface. Reprinted with permission from Ref. 43, Copyright 2023, American Chemical Society.

CeO$_2$ paired with CdWO$_4$[83] or BiVO$_4$[84] functions similarly in S-scheme catalysts, with electron transfer from the CB of the higher work function semiconductor to the CeO$_2$ VB, and electrons from the CeO$_2$ CB reducing CO$_2$. The opposite arrangement is also possible with CeO$_2$, where a lower work-function semiconductor performs CO$_2$ reduction and the balancing reactions (e.g., $2H_2O \rightarrow 4H^+ + O_2$) will occur at the CeO$_2$ VB, as demonstrated in the case of CeO$_2$/LaTiO$_2$N.[85] A more recent work by Zhang et al. utilize CeO$_2$ in this role in an S-scheme photocatalyst, providing evidence of the proposed charge-transport pathway through DFT calculations and in situ XPS measurements.[86]

CeO$_2$-based CO$_2$ reduction catalysts have become more sophisticated and well-understood in recent years, with prominent studies in general agreement on the importance of promoting CO$_2$ adsorption/activation with basic sites, and thwarting carrier recombination with various charge-transport schemes. The actual mechanisms behind charge transfer do not rise to this consensus, however, and elucidation of more fundamental physics at these heterojunctions may be necessary to further optimize these photocatalysts. Notably, there are extreme discrepancies in the reported work-function value for CeO$_2$ in these photocatalysts, ranging from 4.0 eV[86] to 6.67 eV[79] in even the small sample of S-scheme photocatalysts. We anticipate that more advanced probes of charge transfer, in conjunction with computational and model experimental studies, will be needed to definitively establish the proposed schemes and optimize photocatalysts accordingly.

Environmental Remediation/Decontamination Reactions

CeO$_2$ has many properties that make it ideally suited as a catalyst for decontamination/degradation applications. The previously discussed formation of O$_{vac}$ and photoexcitable bandgap act synergistically: the CBof CeO$_2$ is situated above potentials for several reactive oxygen species (ROS), such as hydrogen peroxide (H$_2$O$_2$), superoxide (·O$_2^-$), and hydroxyl radical (·OH), which activate O$_2$ adsorbed on O$_{vac}$ sites.[87] Band positions in comparison to the redox potentials of common ROS are shown in Fig. 11A. The generalized scheme for ROS formation, described by Kusmierek,[88] is shown below:

$$\mathbf{CeO_2 + h\nu \rightarrow CeO_2(e^-_{CB} + h^+_{VB})}$$
$$\mathbf{CeO_2(h^+_{VB}) + H_2O \rightarrow CeO_2 + H^+ + OH^\bullet}$$
$$\mathbf{CeO_2(h^+_{VB}) + OH^- \rightarrow CeO_2 + OH^\bullet}$$
$$\mathbf{CeO_2(e^-_{CB}) + O_2 \rightarrow CeO_2 + O_2^{\bullet-}}$$
$$\mathbf{O_2^{\bullet-} + H^+ \rightarrow HO_2^\bullet}$$
$$\mathbf{2HO_2^\bullet \rightarrow 2H_2O_2 + O_2}$$
$$\mathbf{H_2O_2 + CeO_2(e^-_{CB}) \rightarrow CeO_2 + OH^\bullet + OH^-}$$

Organic dyes such as methylene blue (MB), methyl orange (MO), or acid orange 7 (AO7) are often used as general probes of photocatalytic decontamination activity. Various CeO_2 nanostructures, including nanowires[89] and nanoparticles[90, 91] degrade these dyes under UV excitation. These studies generally implicate ROS photogenerated through CB electrons or VB holes in destruction of the dye molecules.

Table 3. Dye Degradation Catalysts

Material	Catalyst Loading (g L^{-1})	Dye	Abs. Max (nm)	Degradation	Ref.
CeO_2 Nanowires	1.0	Methyl Orange	465	98% @ 100 min.	89
CeO_2 NPs	0.2	Acid Orange 7	484	85% @ 4 hr.	90
CeO_2	1.0	Milling Yellow	(not specified)	100% @ 30 min.	91
Y-doped CeO_2	0.2	Rhodamine B	610	36% @ 100 min.	5
Ca-doped CeO_2	2.0	Methylene Blue	663	84% @ 50 min.	92
Co-doped CeO_2	0.05	Eosin Yellow	510	91% @ 180 min.	93
Cr-doped CeO_2	0.4	Methylene Blue	665	41% @ 100 min. 59% @100 min.* *w/H_2O_2	94
La-doped CeO_2	0.17	Methylene Blue	665	73% @ 30 min.	95
Zr-doped CeO_2	0.1	Bromophenol Blue	591	150 min^{-1}	96
CeO_2	0.06	Acidic Black 10B	620	88% @ 120 min.	97
$Ce_{1-x}Mn_xO_2$	1.0	Naphthol Blue Black	618	70% @ 4 hr.	98
CeO_2/TiO_2	(not specified)	Bromophenol	590	72% @ 3 hr.	99
CeO_2-TiO_2	3.0	Rhodamine B	580	99.9% @ 8 hr.	100
CeO_2-TiO_2	0.1	Methylene Blue	663	96% @ 6 hr.	101
$CeO_2@TiO_2$	0.1	Rhodamine B	521	75% @ 3 hr.	102

The performance of CeO_2 against these dyes can be enhanced through heteroatom doping to modify the surface chemistry or charge-transfer characteristics. Doping CeO_2 with Y^{3+} to generate additional oxygen vacancies is exceptionally effective against Rhodamine B under broadband illumination.[5] We note a key difference in the role of oxygen vacancies between photocatalysis and CeO_2-based thermal catalysts: for photocatalysis, fixed O_{vac} may be beneficial as they act as O_2 adsorption/activation sites, whereas for thermal catalytic reactions mediated by the MvK mechanism (CO oxidation, water–gas shift, etc.), the persistent 3+ sites induced by Gd or Y can reduce overall activity.[4, 103] Other substitutional dopant metals include Ca,[92] Co,[93] Cr,[94] or Zr,[96] which improve photocatalytic activity by suppressing charge recombination. Efforts aiming to dope CeO_2 to improve light absorption in the visible range will be further discussed in a later section.

In a challenge to the traditional view of bandgap excitation leading to ROS formation, Ji et al. observe superior degradation of AO7 under visible light (λ > 420 nm) compared to UV using CeO_2 nanoparticles.[90] The authors conclude that the dye itself, not CeO_2, was photoexcited by visible light. Electron transfer from the dye to the CeO_2 conduction band then generates superoxide molecules responsible for degradation. This mechanism may explain similar observations seen with other dyes under visible illumination, such as Acidic Black 10B[97] and Naphthol Blue Black.[98] Ji et al. also find a trade-off between improved crystallinity and decreased surface area with calcination temperature, resulting in the best degradation rate with CeO_2 calcination at 550 °C (Fig. 11B).[90]

The ROS effectively degrade a wide range of molecules beyond dyes, making CeO_2 well-suited for photocatalytic waste water treatment, particularly degradation of pharmaceuticals.[104] Amoresi et al. study how different nanoscale morphologies of CeO_2 impact activity against the antibiotic ciprofloxacin, finding that hexagonally shaped structures perform best.[105] DFT analysis (Fig. 11C) indicates that the $\langle 110 \rangle$ and $\langle 311 \rangle$ surfaces of CeO_2 have the highest and lowest electron density, respectively, and that having these surfaces simultaneously exposed lowers the overall recombination rate of photoexcited charges.

As previously discussed in the water-splitting section, CeO_2 can be combined with other semiconductors to form Z-scheme photocatalysts. TiO_2/CeO_2 composites have been widely explored in dye degradation applications, both under UV and visible light.[50, 99-102] Improvements over single oxides (CeO_2 or TiO_2) are often attributed to reduced charge recombination and/or greater light absorption at oxide interfaces.

Yan et al. evaluate a Z-scheme CeO_2/TiO_2 nanotube arrays to sterilize both gram-positive and gram-negative bacteria.[106] This Z-scheme heterojunction generates $\cdot O_2^-$ at CeO_2 and $\cdot OH$ at the VB of TiO_2 (Fig. 11D), both of which damage the cell membranes of bacteria, causing leakage of contents and eventual cell death. The CeO_2/TiO_2 nanotube arrays also outperform TiO_2 nanotube arrays or CeO_2 over a TiO_2 mesh (Fig. 11E), and are effective under practical conditions through tests against actual river water.

Organophosphates (OPs) are another class of molecules readily photodecomposed at CeO_2. This class includes many common pesticides, such as parathion and malathion, as well as chemical warfare agents (sarin, soman, VX, etc.). CeO_2 is effective at adsorbing and partially degrading OPs under dark conditions, displacing leaving groups in the OP molecule through hydrolysis,[107] but until recently had not been evaluated for photocatalytic decontamination of OPs. In contrast, abundant scientific literature details how TiO_2 photocatalysts perform against OPs.[108-110]

Novak et al. evaluate CeO_2 aerogels against the chemical warfare simulant dimethylmethylphosphonate (DMMP), finding hydrolysis products under dark conditions and fully mineralized PO_x under UV illumination (390–400 nm).[43] They also elucidate the role of surface chemistry: CeO_2 surfaces with residual Cl perform poorly against DMMP, while Cl-free surfaces, with abundant terminal hydroxyl groups, show greater rates of product formation (schematic in Fig. 11F).

Studies of dye degradation and other environmental applications with CeO_2 are often highly empirical, with adequate experimental data regarding the target reaction but less convincing discussions of underlying mechanisms. Due to the more complex nature of the molecules involved in these remediation applications, their fundamentals are often not as well-understood as the water-splitting or CO_2 reduction reactions discussed earlier. In most cases catalytic turnover – the ability of a site to desorb product and catalyze further reactants – cannot be properly evaluated in typical batch-to-batch trials, limiting long-term stability evaluations. We anticipate that further research will need to proceed on both a fundamental front – with mechanistic studies and molecule degradation analysis – as well as a more applied front – establishing proof of concept reactors more analogous to real-world wastewater treatment schemes.

Visible-Light Sensitization of CeO_2

There are two key principles to exploit when photosensitizing CeO_2 . The bandgap of CeO_2 can be lowered into the visible range through modifying the stoichiometry/exposed facet or by substitutional doping with heteroatoms. Alternatively, metal nanoparticles can be added to the CeO_2 surface to improve visible-light photocatalysis. In both cases, sensitization aims to create photoexcited charges in CeO_2 that would otherwise only be generated under higher energy incident light.

Non-Metal Dopants

The visible-light activity of CeO_2 can be increased by "doping" CeO_2 with itself, namely by increasing the amount of Ce^{3+} sites.[111] Yuán and coworkers synthesize a Confeito-like (star-like) CeO_2 material designated $Ce–O_{2-x}$ that displays an impressive 38.8% Ce^{3+} content leading to a surface plasmon resonance effect (SPR) that red shifts the absorption of CeO_2 to 500 nm. The confeito-CeO_2 oxidizes isopropanol to acetone under visible-light irradiation, while commercial ceria is not effective (Fig. 12).

Similarly, by synthesizing CeO_2 under an oxygen atmosphere, Zhao et al. produce a ceria surface coated with bridging peroxides capable of activating visible light toward the selective oxidation of benzyl alcohol to benzaldehyde.[112] Another study shows that the bandgap energy of CeO_2 can be dramatically altered by the morphology of the CeO_2 particles, from 3.17 eV for hexagonal CeO_2 down to 1.93 eV for cuboidal CeO_2 (Fig. 13) and that this lower bandgap increases UV photocatalytic degradation of MB, however visible-light catalysis was not attempted.[113]

Other non-metal ions also dope CeO_2. A sample doped with Ca^{2+} shows visible-light activation toward methylene-blue degradation.[92] CeO_2 can also be doped with nitrogen for visible-light activation, however special care must be taken with these materials as calcining them above 200 °C replaces N with O_2.[114] This effect can be overcome by running reactions requiring high heat under an ammonia atmosphere; under these conditions these materials are capable of photocatalysis of acetaldehyde using visible light.[49]

Despite several prominent reports of dye-sensitized TiO_2 for photocatalytic reactions,[115-117] to the best of our knowledge this field remains unexplored for CeO_2. Dye-sensitized solar cells (DSSC) have been demonstrated with CeO_2 utilizing N719,[118] rose Bengal,[119] and spinach extract + Eosin-Y dye sensitizers,[120] proving that many organic dyes effectively sensitize CeO_2. Future research exploring photocatalytic reactions with dye-sensitized CeO_2 may be fruitful.

Metal Dopants

The internal structure of CeO_2 can be doped by inclusion of metal ions into the CeO_2 lattice. These substitutions occur during the synthesis of the oxide, where some percentage of Ce atoms are replaced by the additional metal. Because CeO_2 formally contains Ce^{4+} ions, inclusion of M^{2+} or M^{3+} ions leads to additional oxygen vacancies in CeO_2 and an increase in Ce^{3+} sites. These additional oxygen vacancies can serve multiple roles in photocatalysts, not only extending absorption into the visible range but also modifying the surface chemistry to better adsorb reactants on the surface.[121] A summary of dopants added to CeO_2 and their reported effect on the bandgap is shown in Table 2. The mechanism by which the bandgap is lowered through addition of these dopants is commonly cited as either modification of CeO_2 speciation (i.e., more Ce^{3+} sites) or quantum-confinement effects.

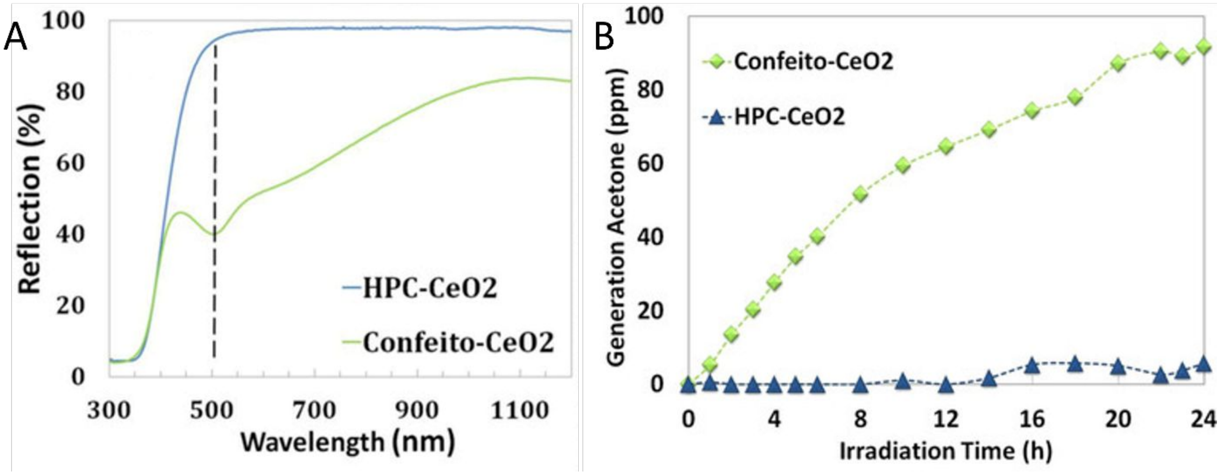

Fig. 12 Comparison of HPC (commercial) CeO_2 and Confeito-CeO_2 for (A) reflectance as a function of wavelength and (B) oxidation of IPA to acetone. Reprinted with permission from Ref. 111, Copyright 2018, Wiley-VCH. xx

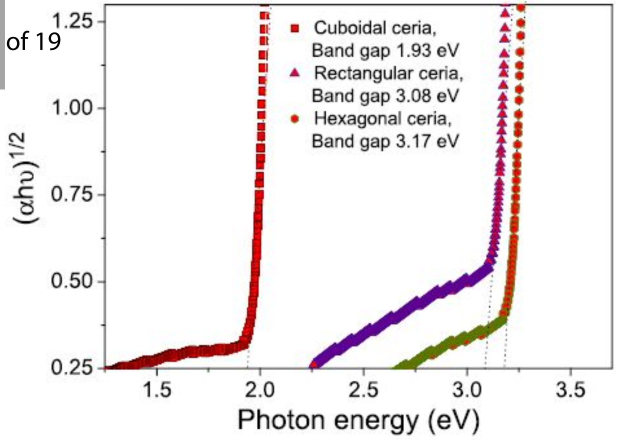

Fig. 13 Tauc plots of cuboidal, rectangular, and hexagonal **CeO_2**. Reprinted with permission from Ref. 113, Copyright 2019, American Chemical Society.

A common set of dopants added to CeO_2 are other lanthanides, as they have a similar atomic radius to Ce and therefore do not cause large disruptions of the lattice while introducing a metal with a different valence and oxidation state. Doping CeO_2 quantum dots with 2%, 4%, and 6% La^{3+} cause a major shift towards visible light, and the resulting particles are capable of dye degradation and antibacterial activity (Fig. 14A).[95] Similarly, doping with Eu^{3+} also enhances photocatalytic performance in the breakdown of formaldehyde relative to pristine CeO_2.[38] The authors find that increasing Eu^{3+} content to 4% reaches peak activity, but further concentration increases up to 8% begin to degrade performance. This effect is attributed to three causes, the 4% Eu^{3+} sample has the largest surface area creating more active sites for substrate reactivity, an enhancement in visible-light absorption, and critically, that 8% Eu has a sufficiently large number of Ce^{3+} sites that they become charge recombination centers rather than charge-separation centers. The Y^{3+}-doped samples also show a dramatic increase in visible-light sensitization up to 50% Y^{3+}, however peak photocatalytic activity for dye degradation is achieved at 10% Y^{3+} inclusion.[5] Not every lanthanide increases visible-light sensitization when doped in CeO_2. Gd^{3+} doping does increase UV light absorption and increases ionic conductivity, however the λ_{max} actually blue shifts in these samples.[131]

Li et al. also investigate doping a variety of transition metals into CeO_2 for photocatalytic water-splitting.[140] Each transition metal surveyed, Cr, Zr, Cu, Co, Fe, and Zn, dramatically increase visible-light activity for the CeO_2 catalyst (Fig. 14B). This increase in activity also increases H_2 production, with Cu giving the highest yield (Fig. 14C). The discrepancy between Cu producing the most H_2 while only having the third highest visible-light absorption is ascribed to the higher strength of the O–H bond during the thermochemical step of the reaction for Cr and Co-doped CeO_2.

From a purely photocatalytic perspective, enhanced light activity leading to high catalytic activities corresponds to the increase in visible-light absorption. A similar trend in visible-light absorption with doped CeO_2 and corresponding dye degradation activity is also found with Ti, Mn, Fe, and Co doping.[125] Co-doped ceria, an effective dye-degradation photocatalyst, absorbs visible light, while increasing the time of electron transfer and leading to slower hole recombination.[93] The authors note a significant nonlinear optical behavior which is enhanced over CeO_2 doped with Co which they attribute to thermal effects, however polaron behavior of the material is a candidate worth exploring.

Doping CeO_2 with Fe increases visible-light absorption up to 30% Fe, reaching a maximum yield in the photocatalytic reduction of CO_2 up to 20% Fe, after which performance declines.[141] A photocatalytic efficiency of 100% was achieved with a 2% Fe-doped CeO_2 produced by flame-spray pyrolysis forming spherical or equiaxed particles for degradation of formic and oxalic acids.[142] Another highly effective Fe-doped CeO_2 in a rose flower–like nanostructure with ≈ 16% Fe was found to be an effective photocatalyst for dye degradation. Each of these Fe-doped catalysts is synthesized in different manners, leading to different morphology and crystal sizes, and each of them shows a different bandgap energy and maximum amount of dopant for peak performance. Further study of these materials is necessary to elucidate which factors are due to reaction condition necessities, morphologies, and dopant concentrations.

Table 4. Summary of metal dopants added to CeO_2 and their reported effects on bandgap.

Dopant	Bandgap (eV)
Ag	2.84 – 3.13,[122] 1.86[123]
Au	2.96 – 3.15[122]
Bi	2.62[124]
Ca	3.36 – 3.51[21]
Cd	2.75[124]
Co	2.69 [125]
Cu	1.15 – 2.47[126], 2.85[127]
Cr	2.52 – 2.60[128]
Er	2.8[129]
Eu	3.33[20]
Fe	2.81,[125] 2.15 – 2.90,[130] 2.7[127]
Gd	2.87 – 3.14[131]
In	2.65 – 2.90[132]
La	3.59 – 3.52[95]
Mn	2.78[125]
N	2.45[34]
Nb	3.09[133]
Ni	3.2[127]
Pb	2.25[124]
Sm	2.45 – 2.80[134]
Ti	2.77[125]
Y	2.62 – 2.82[5]
Y_6WO_{12}	3.21 – 3.31[135]
Yb	2.8[129]
ZnO	2.9[136]
Zr	3.6 – 3.7,[137] 3.3 – 3.4,[96] 3.08,[138] 2.54 – 2.66[139]

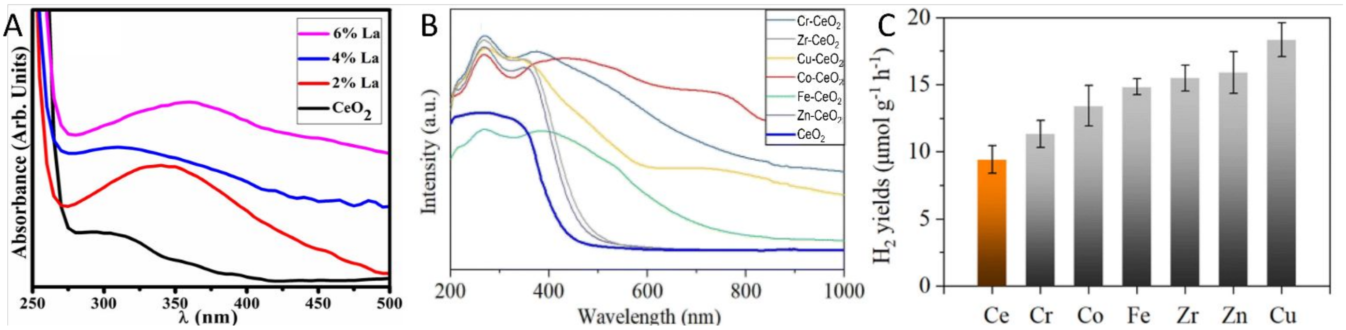

Fig. 14 (A) UV–Vis absorption spectra of CeO_2 and CeO_2 doped with La. Reprinted with permission from Ref. 95, Copyright 2023, American Chemical Society. UV–Vis absorption spectra (B) and H_2 yields (C) of CeO_2 doped with various transition metals. Reprinted with permission from Ref. 140, Copyright 2023, Royal Society of Chemistry.

Cr has been effective in doping CeO_2, but the photocatalytic efficiencies are typically lower than other metals. This process can be improved by using H_2O_2.[94] Other metal dopants, such as Cd, instead blue shift the absorption band of CeO_2, decreasing visible-light sensitization but increasing UV photocatalysis.[143] Cu doping of CeO_2 leads to an effective CO_2 reduction catalyst by lowering the bandgap and increasing oxygen vacancies, although caution should be applied as during calcination some amount of Cu segregates to the surface of the catalyst to form CuO particles, and it is difficult to differentiate where the enhanced activity comes from.[144] When CeO_2 is doped with Mn, a room-temperature ferromagnetic property is found that coincides with the increased visible-light absorption, which represents an interesting avenue to explore the properties of these materials.[145]

Typically, noble metals are incorporated onto CeO_2 to form light-stimulated plasmons, however they are effective as lattice dopants as well. Pd incorporation into CeO_2 enhances visible-light absorption dramatically from 0.5 % to 5 % at.% and is effective for photocatalytic dye degradation, photoelectrochemical current production, and as a photocatalytic antibacterial agent.[146]

To briefly summarize, a large variety of metals can be doped into CeO_2 allowing access to a diverse range of visible light. These metals specialize in the catalysis of various reactions, and choosing the proper dopant, in the proper concentration, in the proper morphology of CeO_2 is key to maximizing catalytic performance.

Plasmonic Sensitization

Surface plasmons are collective electron oscillations at the interface between two materials. In metallic nanoparticles, plasmonic resonance can greatly increase interactions between the material and incident photons, leading to immense research interest in applications that leverage these unique properties.[147] Since plasmonic resonance requires free electrons, noble metals Au and Ag are commonly employed, but more affordable transition metals, notably Cu, can display plasmon resonance as well. Plasmon resonance can be tuned through nanoparticle size, composition, and surrounding medium. The ability of these metallic nanoparticles to absorb visible light and potentially inject charges makes them excellent complementary materials to semiconducting oxides that are otherwise only excited in the UV range.[148, 149] A typical scheme showing charge transfer from plasmonic nanoparticle to semiconductor is shown in Fig. 15A.[150]

CeO_2 paired with plasmonic nanoparticles can photocatalyze many of the previously discussed reactions, notably degradation of dyes and other organic pollutants. A Ag/CeO_2 catalyst with well-dispersed Ag nanoparticles also shows efficient catalysis for MB through a mechanism involving hydroxy radicals in a basic environment.[151] Compared to pristine CeO_2, Ag/CeO_2 displays dramatically improved light absorption in the visible region due to the plasmon resonance of Ag (Fig. 15B). Consistent with the previously discussed heterojunctions above, this study also observes that their increase in efficiency is due to a large separation in charge after photo-irradiation as shown by quenching of the CeO_2 photoluminescence emission spectra. Other work observes similar performance against organic dyes under visible light utilizing plasmonic Ag in core–shell structures,[36] Ag decorated on CeO_2 nanoparticles,[123] or Ag-decorated CeO_2 nanorods.[152]

Although many studies achieve performance improvements over pure CeO_2 through decoration with plasmonic nanostructures, the mechanism of enhancement is often difficult to determine. Dao et al. demonstrate photocatalytic HER using plasmonic Au/CeO_2 core–shell nanoparticles, finding that Au improves H_2 generation rate by an order of magnitude.[35] They propose four possible mechanisms (Fig. 15C) to explain the effects: (1) electromagnetic radiation (EMR) released by Au plasmon-generated electron–hole pairs in CeO_2, (2) hot electron transfer (HET) from photoexcited electrons in Au to CeO_2, (3) plasmon-resonant energy transfer (PRET) in overlapping spectral regions of Au and CeO_2 absorption, and (4) increased Ce^{3+} states at the Au/CeO_2 interface that absorb visible light and further promote charges to Ce^{4+} states.

Cresi et al. attempt to probe charge transfer in plasmonic systems using a model $Ag@CeO_2$ system with a visible pump (430 nm) and free-electron laser probe.[51] Based on changes in the time-resolved X-ray absorption (TRXAS) spectra corresponding to Ce^{3+} states, they conclude plasmon-mediated electron injection from Ag to the Ce *4f* localized states occurs extremely quickly (~200 fs), and that the photoexcited *4f* charges are relatively long-lived; no decay is observed up to 1 ps.

Although electron transfer through plasmon resonance has been confirmed to occur, it may not always be the dominant factor in photocatalysis. Ullah et al. compared Co and Cu nanoparticles over CeO_2 for CO_2 methanation under dark, blue-light, and green-light conditions, finding that both Co and Cu create enhancement under certain conditions. Cu/CeO_2 shows the highest photoenhancement under green light (Fig. 15D), corresponding to the plasmon resonance of Cu^0, but Co/CeO_2 performs better under blue light, showing that enhancement must originate from direct photoactivation of adsorbed species rather than any plasmon resonance.[153] Plasmonic Cu over CeO_2 has been studied for methanol stream-reforming as well, where photoenhancements are attributed to a combination of photoexcitation and thermal effects.[154]

Plasmonic nanoparticles can also enhance oxide heterojunctions for CO_2 reduction. In the case of Ag-CeO_2-ZnO Z-scheme photocatalyst, the plasmonic Ag fulfilled two roles, sensitizing the high bandgap oxides to visible light and acting as a solid-state charge mediator.[155] Using EPR in conjunction with the radical-trapping molecule DMPO, formation of both ·OH and $\cdot O_2^-$ under a simulated solar spectrum greatly increases with the presence of Ag compared to either of the pure oxides (Fig. 15E).

Selective oxidations are achievable with plasmonic Au on CeO_2, where after photoexcitation the electron is passed from Au to Ce, and the Au in turn oxidizes a substrate like benzyl alcohol to benzaldehyde. The amount of metal used is important in these catalysts, where excess amounts of the metal begin to serve as recombination centres absorbing charge rather than contributing to it.[156] With careful catalytic design, these effects can be enhanced as shown by Tanaka et al., where a multistep photo deposition of Au allows for fewer large Au particles and thus increased beneficial effects of increasing Au concentration past single deposition methods.[157] Pt metal-doped CeO_2 is also a selective catalyst for alcohol oxidations, and some clever design by Jiang et al. utilize a Pt-core and Pt-Ag core with a porous CeO_2 shell in a metal yolk/porous CeO_2 shell design to provide a void space for substrate diffusion.[158]

Some catalysts exploit these differences in bandgap energy with three or more component systems, such as the C–Cl bond cleavage achieved by Zhang et al. utilizing a Pd/Au/porous nanorod(PN)-CeO_2 catalyst where PN-CeO_2 transfers an electron first to the Au nanoparticle and then to the Pd nanocrystal, which activates the aryl chloride.[159] The original hole in the PN-CeO_2 VB simultaneously activates an aryl boronic acid. These two activated species then combine to form a biphenyl in a photocatalytic Suzuki–Miyaura coupling (Fig. 15F).

Metal nanoparticles are clearly effective at promoting many photocatalytic reactions over CeO_2, but we caution against attributing all enhancements to plasmon resonance. As we discussed in the case of Co/CeO_2, enhancement may derive from photoactivation of adsorbed species.[153] Recent work also establishes that plasmonic metals may aid in catalysis simply by creating localized hot spots to drive thermal catalysis.[160] Verification of injection to the Ce *4f* band – through observation of Ce^{3+} – may

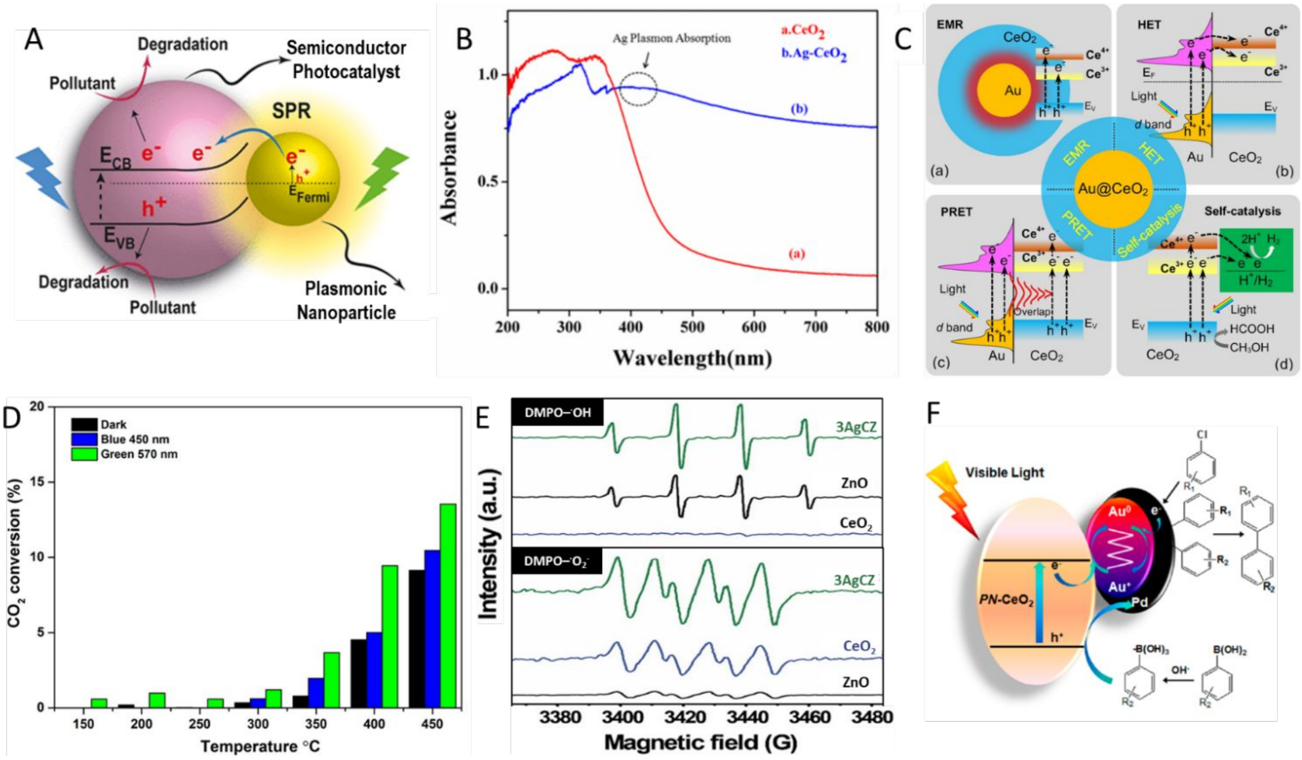

Fig. 15 (A) Illustration of a plasmonic metal–semiconductor junction. Reprinted with permission from Ref. 150, Copyright 2023, American Chemical Society. (B) UV-vis of CeO_2 and Ag-CeO_2, showing significant absorption in the visible region after plasmonic Ag is added. Reprinted with permission from Ref. 151, Copyright 2016, Elsevier. (C) Potential photoenhancement mechanisms for Au@CeO_2. Reprinted with permission from Ref. 134, Copyright 2021, Elsevier. (D) CO_2 conversion as a function of temperature under dark, blue light, or green light conditions. Reprinted with permission from Ref. 153 Copyright 2020, American Chemical Society. (E) EPR signals tracking DMPO-·OH and DMPO-$\cdot O_2^-$ adducts over ZnO, CeO_2, and 3AgCN. Reprinted with permission from Ref. 155, Copyright 2021, American Chemical Society. (F) Schematic of the proposed Suzuki–Miranda coupling reaction over Pd/Au/*PN*-CeO_2 catalysts. Reprinted with permission from Ref. 159, Copyright 2015, American Chemical Society.

become a standard procedure for works asserting plasmonic sensitization of CeO_2.

Summary and Future Research Directions

Nanostructured CeO_2-based photocatalysts show tremendous promise in many industrially and environmentally relevant reactions. Compared to other lanthanides, cerium is a cheap and abundant element, and many routes toward nanostructured CeO_2 are relatively simple and scalable. The most studied reactions photocatalyzed by CeO_2 are those related to water-splitting (HER/OER), reduction of CO_2, or decontamination of toxic molecules, particularly those in wastewater. Common strategies to improve the performance of CeO_2 photocatalysts include heteroatom substitution in the CeO_2 lattice, creating heterojunctions with other photocatalytic oxides, or incorporating plasmonic metals onto the CeO_2 surface. These methods are clearly successful in both thwarting charge recombination and extending the photoactivity of CeO_2 well into the visible range. Balancing these changes to the CeO_2 structure with changes to morphology and oxygen vacancy sites is challenging, and the results can be difficult to predict.

Despite the rapid advancement of these nanomaterials, much of the physics regarding how these photocatalysts operate remains ambiguous. CeO_2 differs from conventional semiconductors in that what is traditionally considered the conduction band for these materials is actually a localized polaron in the *4f* state rather than a freely conducting electron in the *5d* state. This heavy electron, dressed by a phonon, causes a lattice distortion in CeO_2 preventing its free flow, because to move it requires distorting the lattice in its new position as the previous site relaxes. Some DFT methods to simulate the structure of CeO_2 are incapable of producing the correct polaron result. The pervasive use of Tauc plots – a method that presumes excitation between parabolically shaped bands – further muddles the physics of photoexcitation in CeO_2. Perhaps as a consequence, charge-transfer schemes between CeO_2 and other semiconductors or plasmonic metals are usually inferred rather than rigorously probed. We have highlighted recent ultrafast spectroscopic results that prove that excitation to the *4f* state and polaron formation occur upon UV irradiation and confirmed this polaron formation through a sophisticated DFT method that accounts for localization/correlation on both *d* and *f* orbitals. This method reproduces the fundamental band gap, and the position of the localized *f*-states within the band gap. The calculated energy position of an induced polaron is also in good agreement with spectroscopy, further confirming the character of the photoexcited state.

Recognizing the difference between this localized excited state and conventional semiconductors will be vital to exploiting the remarkable intrinsic properties of these materials to realize more active and more efficient catalysts. Understanding the way that the polaron moves in relation to oxygen vacancies can help ensure that the local geometry is tuned toward charge transfer. A full understanding of the photophysics of polaron generation and transport is essential to resolve the role of dopants, morphology, and oxygen vacancies in the photoexcitation and reactivity of CeO_2-based catalysts. Indeed, further physical characterization and DFT studies can disentangle the role of dopants in dictating the physics that govern oxygen vacancy and polaron formation. Both ultrafast optical techniques and in situ X-ray spectroscopy will verify injection into the *4f* state and elucidate transfer pathways. This improved fundamental understanding will eventually pave the way for further practical improvements, as polaron tuning for heterojunctions and plasmons could open up new catalytic avenues. In short, we hope with this review to bridge some of the gap between the unique physical properties of CeO_2-based materials and the guided materials design as a means toward understanding of CeO_2 as a potent photocatalyst.

Author Contributions

A.E.H. researched and wrote sections regarding visible-light sensitization. T.J.M and A.D.D. researched and wrote sections regarding fundamental optical properties of CeO_2. M.D.J. wrote the section regarding computational studies and developed the original figures presented. D.R.R. and P.A.D. outlined the original manuscript ideas and extensively edited the final submission. T.G.N. coordinated the group writing efforts and wrote the section regarding common reactions over CeO_2.

Conflicts of interest

There are no conflicts to declare.

Acknowledgements

This work was supported by the U.S. Office of Naval Research. A.E.H. and T.J.M are Naval Research Laboratory/National Research Council Postdoctoral Associates. The authors acknowledge funding provided by the Defense Threat Reduction Agency (DTRA, HDTRA CB10992).

References

1. A. A. Yaroshevsky, *Geochem. Int.*, 2006, **44**, 48-55.
2. L. Wu, H. J. Wiesmann, A. R. Moodenbaugh, R. F. Klie, Y. Zhu, D. O. Welch and M. Suenaga, *Phys. Rev. B*, 2004, **69**, 125415.
3. H. Hojo, K. Hirota, S. Ito and H. Einaga, *Adv. Mater. Interfaces*, 2023, **10**, 2201954.
4. T. G. Novak, P. A. DeSario, T. H. Brintlinger, R. H. DeBlock, J. W. Long and D. R. Rolison, *ACS Sustain. Chem. Eng.*, 2023, **11**, 2853-2860.
5. A. D. Liyanage, S. D. Perera, K. Tan, Y. Chabal and K. J. Balkus, Jr., *ACS Catal.*, 2014, **4**, 577-584.
6. K. Sun, W. Lu, M. Wang and X. Xu, *Appl. Catal., A*, 2004, **268**, 107-113.
7. F. Jiang, S. Wang, B. Liu, J. Liu, L. Wang, Y. Xiao, Y. Xu and X. Liu, *ACS Catal.*, 2020, **10**, 11493-11509.

8. G. Spezzati, A. D. Benavidez, A. T. DeLaRiva, Y. Su, J. P. Hofmann, S. Asahina, E. J. Olivier, J. H. Neethling, J. T. Miller, A. K. Datye and E. J. M. Hensen, *Appl. Catal., B*, 2019, **243**, 36-46.
9. Z. Tan, G. Li, H.-L. Chou, Y. Li, X. Yi, A. H. Mahadi, A. Zheng, S. C. Edman Tsang and Y.-K. Peng, *ACS Catal.*, 2020, **10**, 4003-4011.
10. C. Zhu, X. Wei, W. Li, Y. Pu, J. Sun, K. Tang, H. Wan, C. Ge, W. Zou and L. Dong, *ACS Sustain. Chem. Eng.*, 2020, **8**, 14397-14406.
11. C. Zang, X. Zhang, S. Hu and F. Chen, *Appl. Catal., B*, 2017, **216**, 106-113.
12. Q. Li, L. Song, Z. Liang, M. Sun, T. Wu, B. Huang, F. Luo, Y. Du and C.-H. Yan, *Adv. Energy Sustainability Res.*, 2021, **2**, 2000063.
13. M. A. Salaev, A. A. Salaeva, T. S. Kharlamova and G. V. Mamontov, *Appl. Catal., B*, 2021, **295**, 120286.
14. A. A. Fauzi, A. A. Jalil, N. S. Hassan, F. F. A. Aziz, M. S. Azami, I. Hussain, R. Saravanan and D. V. N. Vo, *Chemosphere*, 2022, **286**, 131651.
15. S. A. B. Gilani, F. Naseeb, A. Kiran, M. Umar Ihsan, J. Iqbal, H. Muhammad Asif Javed, H. N. Bhatti, A. M. Karami, S. Hussain and M. ShabirMahr, *Opt. Mater.*, 2024, **148**, 114871.
16. F. Wang, F. Zeng, Z. Yu, C. Chen, X. Huang, W. Zhang, Y. Lan and J. Li, *Surf. Interfaces*, 2024, **46**, 103889.
17. X. Li, M. Wang, R. Wang, Y. Wang, M. Zhu, L. Zhang and J. Shi, *ACS Nano*, 2024, **18**, 5741-5751.
18. R. Jin and T. Higaki, *Comm. Chem.*, 2021, **4**, 28.
19. R. V. Nair, V. S. Gummaluri, M. V. Matham and V. C, *J. Phys. D: Appl. Phys.*, 2022, **55**, 313003.
20. Z. Wang, Z. Quan and J. Lin, *Inorg. Chem.*, 2007, **46**, 5237-5242.
21. L. Truffault, M.-T. Ta, T. Devers, K. Konstantinov, V. Harel, C. Simmonard, C. Andreazza, I. P. Nevirkovets, A. Pineau, O. Veron and J.-P. Blondeau, *Mater. Res. Bull.*, 2010, **45**, 527-535.
22. S. Samiee and E. K. Goharshadi, *Mater. Res. Bull.*, 2012, **47**, 1089-1095.
23. C. W. M. Castleton, A. Lee and J. Kullgren, *J. Phys. Chem. C*, 2019, **123**, 5164-5175.
24. M. Melchionna and P. Fornasiero, *Mater. Today*, 2014, **17**, 349-357.
25. L. Lin, X. Ma, S. Li, M. Wouters and V. Hessel, *Front. Chem. Sci. Eng.*, 2019, **13**, 501-510.
26. J. Klein, L. Kampermann, B. Mockenhaupt, M. Behrens, J. Strunk and G. Bacher, *Adv. Funct. Mater.*, 2023, **33**, 2304523.
27. D. Damatov, S. M. Laga, E. A. Mader, J. Peng, R. G. Agarwal and J. M. Mayer, *Inorg. Chem.*, 2018, **57**, 14401-14408.
28. J. S. Pelli Cresi, L. Di Mario, D. Catone, F. Martelli, A. Paladini, S. Turchini, S. D'Addato, P. Luches and P. O'Keeffe, *J. Phys. Chem. Lett.*, 2020, **11**, 5686-5691.
29. E. Spurio, J. S. Pelli Cresi, G. Ammirati, S. Pelatti, A. Paladini, S. D'Addato, S. Turchini, P. O'Keeffe, D. Catone and P. Luches, *ACS Photonics*, 2023, **10**, 1566-1574.
30. S. Ghosh, B. Pham, M. Madhu and B. Kohler, *J. Phys. Chem. C*, 2023, **127**, 21593-21602.
31. M. Ramachandran, R. Subadevi and M. Sivakumar, *Vacuum*, 2019, **161**, 220-224.
32. A. Chitsaz, M. Jalilpour and M. Fathalilou, *Int. J. Mater. Res.*, 2013, **104**, 511-514.
33. H. Yang, L. Jia, J. Haraguchi, Y. Wang, B. Xu, Q. Zhang, Z. Nan, M. Zhang and T. Ohno, *Catal. Sci. Technol.*, 2022, **12**, 5203-5209.
34. Z. Shen, Q. Xia, Y. Li, C. Yin, Z. Ge, X. Li and Y. Wang, *J. CO2 Util.*, 2020, **39**, 101176.
35. D. V. Dao, T. T. D. Nguyen, P. Uthirakumar, Y.-H. Cho, G.-C. Kim, J.-K. Yang, D.-T. Tran, T. D. Le, H. Choi, H. Y. Kim, Y.-T. Yu and I.-H. Lee, *Appl. Catal., B*, 2021, **286**, 119947.
36. L. Wu, S. Fang, L. Ge, C. Han, P. Qiu and Y. Xin, *J. Hazard. Mater.*, 2015, **300**, 93-103.
37. S.-W. Lin, M.-H. Tong, Y.-X. Chen, R. Chen, H.-P. Zhao, X. Jiang, K. Yang and C.-Z. Lu, *ACS Appl. Energy Mater.*, 2023, **6**, 1093-1102.
38. Y. Huang, B. Long, M. Tang, Z. Rui, M.-S. Balogun, Y. Tong and H. Ji, *Appl. Catal., B*, 2016, **181**, 779-787.
39. M. Sridharan, P. Kamaraj, Y. S. Huh, S. Devikala, M. Arthanareeswari, J. A. Selvi and E. Sundaravadivel, *Catal. Sci. Technol.*, 2019, **9**, 3686-3696.
40. Z. Liu, Y. Zhuang, L. Dong, H. Mu, D. Li, F. Zhang, H. Xu and H. Xie, *ACS Appl. Energy Mater.*, 2023, **6**, 7722-7736.
41. S. K. Jha, C. N. Kumar, R. P. Raj, N. S. Jha and S. Mohan, *Electrochim. Acta*, 2014, **120**, 308-313.
42. A. E. Gash, T. M. Tillotson, J. H. Satcher Jr, L. W. Hrubesh and R. L. Simpson, *J. Non-Cryst. Solids*, 2001, **285**, 22-28.
43. T. G. Novak, R. B. Balow, M. R. Buck, D. R. Rolison and P. A. DeSario, *ACS Appl. Nano Mater.*, 2023, **6**, 3075-3084.
44. T. G. Novak, P. A. DeSario, M. D. Johannes, T. H. Brintlinger, R. H. DeBlock, J. W. Long, C. N. Chervin, R. M. Stroud and D. R. Rolison, *Chem. Mater.*, 2022, **34**, 5644-5653.
45. W. Li, L. Jin, F. Gao, H. Wan, Y. Pu, X. Wei, C. Chen, W. Zou, C. Zhu and L. Dong, *Appl. Catal., B*, 2021, **294**, 120257.
46. D. Sharma, V. R. Satsangi, R. Shrivastav, U. V. Waghmare and S. Dass, *Int. J. Hydrogen Energy*, 2016, **41**, 18339-18350.
47. N. Celebi, F. Arlı, F. Soysal and K. Salimi, *Mater. Today Energy*, 2021, **21**, 100765.
48. Y. Wang, B. Li, C. Zhang, L. Cui, S. Kang, X. Li and L. Zhou, *Appl. Catal., B*, 2013, **130-131**, 277-284.
49. A. B. Jorge, Y. Sakatani, C. Boissière, C. Laberty-Roberts, G. Sauthier, J. Fraxedas, C. Sanchez and A. Fuertes, *J. Mater. Chem.*, 2012, **22**, 3220-3226.
50. X. Wang, Y. Jin and X. Liang, *Nanotechnology*, 2017, **28**, 505709.
51. J. S. Pelli Cresi, E. Principi, E. Spurio, D. Catone, P. O'Keeffe, S. Turchini, S. Benedetti, A. Vikatakavi, S. D'Addato, R. Mincigrucci, L. Foglia, G. Kurdi, I. P. Nikolov, G. De Ninno, C. Masciovecchio, S. Nannarone, J. Kopula Kesavan, F. Boscherini and P. Luches, *Nano Lett.*, 2021, **21**, 1729-1734.
52. H. C. Herper, O. Y. Vekilova, S. I. Simak, I. Di Marco and O. Eriksson, *J. Phys.: Condens. Matter*, 2020, **32**, 215502.
53. I. A. Vladimir, F. Aryasetiawan and A. I. Lichtenstein, *J. Phys.: Condens. Matter*, 1997, **9**, 767.
54. C. W. M. Castleton, J. Kullgren and K. Hermansson, *J. Chem. Phys.*, 2007, **127**, 244704.
55. B. Dong, L. Li, Z. Dong, R. Xu and Y. Wu, *Int. J. Hydrogen Energy*, 2018, **43**, 5275-5282.
56. K. Maeda, *ACS Catal.*, 2013, **3**, 1486-1503.
57. Y. Zhao, X. Linghu, Y. Shu, J. Zhang, Z. Chen, Y. Wu, D. Shan and B. Wang, *J. Environ. Chem. Eng.*, 2022, **10**, 108077.
58. Y. Ma, Y. Bian, Y. Liu, A. Zhu, H. Wu, H. Cui, D. Chu and J. Pan, *ACS Sustain. Chem. Eng.*, 2018, **6**, 2552-2562.

59. Y. Wang, X. Hao, L. Zhang, Y. Li and Z. Jin, *Energy Fuels*, 2020, **34**, 2599-2611.
60. S. Sultana, S. Mansingh, M. Scurrell and K. M. Parida, *Inorg. Chem.*, 2017, **56**, 12297-12307.
61. H. Yu, J. Xu, C. Yin, Z. Liu and Y. Li, *J. Solid State Chem.*, 2019, **272**, 102-112.
62. M. Waqas, B. Yang, L. Cao, X. Zhao, W. Iqbal, K. Xiao, C. Zhu and J. Zhang, *Catal. Sci. Technol.*, 2019, **9**, 5322-5332.
63. A. Krishnan, S. Beena and M. Chandran, *Mater. Today Proc.*, 2019, **18**, 4968-4976.
64. X. Cui, Z. Liu, G. Li, M. Zhang, Y. Song and J. Wang, *Int. J. Hydrogen Energy*, 2019, **44**, 23921-23935.
65. J. Qian, Z. Chen, F. Chen, Y. Wang, Z. Wu, W. Zhang, Z. Wu and P. Li, *Inorg. Chem.*, 2018, **57**, 14532-14541.
66. G. Swain, S. Sultana, B. Naik and K. Parida, *ACS Omega*, 2017, **2**, 3745-3753.
67. S. Lin, H. Huang, T. Ma and Y. Zhang, *Adv. Sci.*, 2021, **8**, 2002458.
68. J. Qi, K. Zhao, G. Li, Y. Gao, H. Zhao, R. Yu and Z. Tang, *Nanoscale*, 2014, **6**, 4072-4077.
69. D. H. Seo, S. Y. Hong, T. H. You, A. Sivanantham and I. S. Cho, *Chem. Eng. J.*, 2022, **450**, 137917.
70. A. Das, M. Patra, M. Kumar P, M. Bhagavathiachari and R. G. Nair, *J. Alloys Compd.*, 2021, **858**, 157730.
71. Y. Tan, S. Zhang, R. Shi, W. Wang and K. Liang, *Int. J. Hydrogen Energy*, 2016, **41**, 5437-5444.
72. C. Han, L. Yan, W. Zhao and Z. Liu, *Int. J. Hydrogen Energy*, 2017, **42**, 12276-12283.
73. A. Hezam, K. Namratha, Q. A. Drmosh, D. Ponnamma, J. Wang, S. Prasad, M. Ahamed, C. Cheng and K. Byrappa, *ACS Appl. Nano Mater.*, 2020, **3**, 138-148.
74. M. Wang, M. Shen, X. Jin, J. Tian, Y. Zhou, Y. Shao, L. Zhang, Y. Li and J. Shi, *Nanoscale*, 2020, **12**, 12374-12382.
75. Y. Pu, Y. Luo, X. Wei, J. Sun, L. Li, W. Zou and L. Dong, *Appl. Catal., B*, 2019, **254**, 580-586.
76. P. K. Prajapati, D. Garg, A. Malik, D. Kumar, V. Amoli and S. L. Jain, *J. Environ. Chem. Eng.*, 2022, **10**, 108147.
77. M. Liang, T. Borjigin, Y. Zhang, B. Liu, H. Liu and H. Guo, *Appl. Catal., B*, 2019, **243**, 566-575.
78. M. Li, L. Zhang, M. Wu, Y. Du, X. Fan, M. Wang, L. Zhang, Q. Kong and J. Shi, *Nano Energy*, 2016, **19**, 145-155.
79. L. Cheng, X. Yue, J. Fan and Q. Xiang, *Adv. Mater.*, 2022, **34**, 2200929.
80. Q. Xu, L. Zhang, B. Cheng, J. Fan and J. Yu, *Chem*, 2020, **6**, 1543-1559.
81. Y. Kumar, A. Sudhaik, K. Sharma, Sonu, P. Raizada, A. Aslam Parwaz Khan, V.-H. Nguyen, T. Ahamad, P. Singh and A. M. Asiri, *J. Photochem. Photobiol., A*, 2023, **435**, 114326.
82. K. Sharma, A. Sudhaik, P. Raizada, P. Thakur, X. M. Pham, Q. Van Le, V.-H. Nguyen, T. Ahamad, S. Thakur and P. Singh, *Environ. Sci. Pollut. Res.*, 2023, **30**, 124902-124920.
83. A. Bahadoran, S. Ramakrishna, S. Masudy-Panah, J. R. De Lile, J. Gu, Q. Liu and Y. K. Mishra, *Ind. Eng. Chem. Res.*, 2022, **61**, 10931-10944.
84. J. Geng, S. Guo, Z. Zou, Z. Yuan, D. Zhang, X. Yan, X. Ning and X. Fan, *Fuel*, 2023, **333**, 126417.
85. P. Lin, L. Xiao, Y. Lu, Z. Zhang, X. Wang and W. Su, *ChemCatChem*, 2022, **14**, e202201041.
86. N. Zhang, Y.-G. Luo, Y.-H. Chen, J.-Y. Zhang, H. Wang and Z.-J. Liu, *ACS Sustain. Chem. Eng.*, 2023, **11**, 4813-4824.
87. M. Li, P. Wang, Z. Ji, Z. Zhou, Y. Xia, Y. Li and S. Zhan, *Appl. Catal., B*, 2021, **289**, 120020.
88. E. Kusmierek, *Catalysts*, 2020, **10**, 439.
89. A. Phuruangrat, S. Thongtem and T. Thongtem, *Mater. Lett.*, 2017, **196**, 61-63.
90. P. Ji, B. Tian, F. Chen and J. Zhang, *Environ. Technol.*, 2012, **33**, 467-472.
91. S. Tambat, S. Umale and S. Sontakke, *Mater. Res. Bull.*, 2016, **76**, 466-472.
92. V. Ramasamy, V. Mohana and V. Rajendran, *OpenNano*, 2018, **3**, 38-47.
93. S. E. George, M. George, J. Alex, L. K. Joy, A. Aravind, D. Sajan, A. Thakur, S. Hussain and G. Vinitha, *Ceram. Int.*, 2020, **46**, 13932-13940.
94. I. Y. Habib, J. Burhan, F. Jaladi, C. M. Lim, A. Usman, N. T. R. N. Kumara, S. C. E. Tsang and A. H. Mahadi, *Catal. Today*, 2021, **375**, 506-513.
95. A. Shahzadi, S. Moeen, A. D. Khan, A. Haider, J. Haider, A. Ul-Hamid, W. Nabgan, I. Shahzadi, M. Ikram and A. Al-Shanini, *ACS Omega*, 2023, **8**, 8605-8616.
96. R. Bakkiyaraj, M. Balakrishnan, G. Bharath and N. Ponpandian, *J. Alloys Compd.*, 2017, **724**, 555-564.
97. Y. Zhai, S. Zhang and H. Pang, *Mater. Lett.*, 2007, **61**, 1863-1866.
98. P. Borker and A. V. Salker, *Mater. Chem. Phys.*, 2007, **103**, 366-370.
99. S. Ameen, M. Shaheer Akhtar, H.-K. Seo and H.-S. Shin, *Chem. Eng. J.*, 2014, **247**, 193-198.
100. K. Kasinathan, J. Kennedy, M. Elayaperumal, M. Henini and M. Malik, *Sci. Rep.*, 2016, **6**, 38064.
101. B. Moongraksathum and Y.-W. Chen, *J. Sol-Gel Sci. Technol.*, 2017, **82**, 772-782.
102. L. Zhang, J. Zhang, H. Jiu, X. Zhang and M. Xu, *J. Mater. Sci.*, 2015, **50**, 5228-5237.
103. L. Ilieva, I. Ivanov, P. Petrova, G. Munteanu, Y. Karakirova, J. W. Sobczak, W. Lisowski, E. M. Anghel, Z. Kaszkur and T. Tabakova, *Int. J. Hydrogen Energy*, 2020, **45**, 26286-26299.
104. J. Iqbal, N. S. Shah, Z. U. H. Khan, M. Rizwan, B. Murtaza, F. Jamil, A. Shah, A. Ullah, Y. Nazzal and F. Howari, *J. Water Process Eng.*, 2022, **49**, 103130.
105. R. A. C. Amoresi, R. C. Oliveira, N. L. Marana, P. B. de Almeida, P. S. Prata, M. A. Zaghete, E. Longo, J. R. Sambrano and A. Z. Simões, *ACS Appl. Nano Mater.*, 2019, **2**, 6513-6526.
106. H. Yan, R. Wang, R. Liu, T. Xu, J. Sun, L. Liu and J. Wang, *Appl. Catal., B*, 2021, **291**, 120096.
107. D. A. Chen, J. S. Ratliff, X. Hu, W. O. Gordon, S. D. Senanayake and D. R. Mullins, *Surf. Sci.*, 2010, **604**, 574-587.
108. J. A. Moss, S. H. Szczepankiewicz, E. Park and M. R. Hoffmann, *J. Phys. Chem. B*, 2005, **109**, 19779-19785.
109. J. Henych, A. Mattsson, J. Tolasz, V. Štengl and L. Österlund, *Catal. Sci. Technol.*, 2019, **9**, 1816-1824.
110. P. A. DeSario, W. O. Gordon, A. Balboa, A. M. Pennington, C. L. Pitman, M. McEntee and J. J. Pietron, *ACS Appl. Mater. Interfaces*, 2021, **13**, 12550-12561.
111. S. Yuán, B. Xu, Q. Zhang, S. Liu, J. Xie, M. Zhang and T. Ohno, *ChemCatChem*, 2018, **10**, 1267-1271.
112. Z. Cui, H. Zhou, G. Wang, Y. Zhang, H. Zhang and H. Zhao, *New J. Chem.*, 2019, **43**, 7355-7362.
113. D. Majumder, I. Chakraborty, K. Mandal and S. Roy, *ACS Omega*, 2019, **4**, 4243-4251.
114. C. Mao, Y. Zhao, X. Qiu, J. Zhu and C. Burda, *Phys. Chem. Chem. Phys.*, 2008, **10**, 5633-5638.

115. S. Goulart, L. J. Jaramillo Nieves, A. G. Dal Bó and A. M. Bernardin, *Dyes Pigments*, 2020, **182**, 108654.
116. A. Tiwari, I. Mondal and U. Pal, *RSC Adv.*, 2015, **5**, 31415-31421.
117. S. K. Choi, H. S. Yang, J. H. Kim and H. Park, *Appl. Catal., B*, 2012, **121-122**, 206-213.
118. A. Rajendran and S. Kandasamy, *Mater. Res. Innovations*, 2019, **23**, 15-21.
119. S. A. A. R. Sayyed, N. I. Beedri, V. S. Kadam and H. M. Pathan, *Appl. Nanosci.*, 2016, **6**, 875-881.
120. S. A. A. R. Sayyed, N. I. Beedri and H. M. Pathan, *J. Mater. Sci. Mater. Electron.*, 2017, **28**, 5075-5081.
121. A. Kumar and V. Krishnan, *Adv. Funct. Mater.*, 2021, **31**, 2009807.
122. M. Mittal, A. Gupta and O. P. Pandey, *Solar Energy*, 2018, **165**, 206-216.
123. G. Murugadoss, D. D. Kumar, M. R. Kumar, N. Venkatesh and P. Sakthivel, *Sci. Rep.*, 2021, **11**, 1080.
124. G. Murugadoss, J. Ma, X. Ning and M. R. Kumar, *Inorg. Chem. Commun.*, 2019, **109**, 107577.
125. L. Yue and X.-M. Zhang, *J. Alloys Compd.*, 2009, **475**, 702-705.
126. K. Kumari, R. N. Aljawfi, A. K. Chawla, R. Kumar, P. A. Alvi, A. Alshoaibi, A. Vij, F. Ahmed, M. Abu-samak and S. Kumar, *Ceram. Int.*, 2020, **46**, 7482-7488.
127. M. T. Qamar, S. Iqbal, M. Aslam, A. Alhujaily, A. Bilal, K. Rizwan, H. M. U. Farooq, T. A. Sheikh, A. Bahadur, N. S. Awwad, H. A. Ibrahium, R. S. Almufarij and E. B. Elkaeed, *Front. Chem.*, 2023, **11**.
128. S. K. Alla, E. V. Prasadarao Komarala, R. K. Mandal and N. K. Prasad, *Mater. Chem. Phys.*, 2016, **182**, 280-286.
129. R. Zhao, L. Huan, P. Gu, R. Guo, M. Chen and G. Diao, *J. Power Sources*, 2016, **331**, 527-534.
130. D. Channei, B. Inceesungvorn, N. Wetchakun, S. Ukritnukun, A. Nattestad, J. Chen and S. Phanichphant, *Sci. Rep.*, 2014, **4**, 5757.
131. S. M, R. Rajkumar, T. S and B. S, *Mater. Res. Bull.*, 2012, **47**, 4340-4346.
132. A. Younis, D. Chu, Y. V. Kaneti and S. Li, *Nanoscale*, 2016, **8**, 378-387.
133. T. Shittu and M. Altarawneh, *Nanotechnol. Rev.*, 2022, **11**, 191-203.
134. A. Joseph, A. Ayyappan, T. Subair, M. Pandibayal, S. Nair, R. Ramany, M. Raama Varma and S. Thomas, *ChemistrySelect*, 2023, **8**, e202301020.
135. F. Cheviré, F. Muñoz, C. F. Baker, F. Tessier, O. Larcher, S. Boujday, C. Colbeau-Justin and R. Marchand, *J. Solid State Chem.*, 2006, **179**, 3184-3190.
136. M. Jeyaraj, R. Atchudan, S. Pitchaimuthu, T. N. J. I. Edison and P. Sennu, *Process Saf. Environ. Prot.*, 2021, **156**, 457-464.
137. S. K. Sahoo, M. Mohapatra and S. Anand, *J. Exp. Nanosci.*, 2015, **10**, 1012-1027.
138. M. Zafar, S. Mahmood, H. Shaikh, A. Alhamidi, S. M. Ramay, M. Saleem and S. A. Siddiqi, *Mater. Res. Express*, 2019, **6**, 116321.
139. S. N. Naidi, F. Khan, M. H. Harunsani, A. L. Tan, Y.-M. Kim and M. M. Khan, *Bioprocess Biosyst. Eng.*, 2022, **45**, 279-295.
140. R. Li, C. Wen, K. Yan, T. Liu, B. Zhang, M. Xu and Z. Zhou, *J. Mater. Chem. A*, 2023, **11**, 7128-7141.
141. Y. Wang, F. Wang, Y. Chen, D. Zhang, B. Li, S. Kang, X. Li and L. Cui, *Appl. Catal., B*, 2014, **147**, 602-609.
142. D. Channei, S. Phanichphant, A. Nakaruk, S. S. Mofarah, P. Koshy and C. C. Sorrell, *Catalysts*, 2017, **7**.
143. S. Gnanam and V. Rajendran, *J. Alloys Compd.*, 2018, **735**, 1854-1862.
144. M. Wang, M. Shen, X. Jin, J. Tian, M. Li, Y. Zhou, L. Zhang, Y. Li and J. Shi, *ACS Catal.*, 2019, **9**, 4573-4581.
145. C. Xia, C. Hu, P. Chen, B. Wan, X. He and Y. Tian, *Mater. Res. Bull.*, 2010, **45**, 794-798.
146. S. N. Matussin, F. Khan, M. H. Harunsani, Y.-M. Kim and M. M. Khan, *Catalysts*, 2023, **13**.
147. H. Yu, Y. Peng, Y. Yang and Z.-Y. Li, *npj Comput. Mater.*, 2019, **5**, 45.
148. W. Hou and S. B. Cronin, *Adv. Funct. Mater.*, 2013, **23**, 1612-1619.
149. A. Kumar, P. Choudhary, A. Kumar, P. H. C. Camargo and V. Krishnan, *Small*, 2022, **18**, 2101638.
150. A. Amirjani, N. B. Amlashi and Z. S. Ahmadiani, *ACS Appl. Nano Mater.*, 2023, **6**, 9085-9123.
151. K. Saravanakumar, M. M. Ramjan, P. Suresh and V. Muthuraj, *J. Alloys Compd.*, 2016, **664**, 149-160.
152. J. Liu, L. Zhang, Y. Sun and Y. Luo, *Nanomaterials*, 2021, **11**, 1104.
153. S. Ullah, E. C. Lovell, R. J. Wong, T. H. Tan, J. Scott and R. Amal, *ACS Sustain. Chem. Eng.*, 2020, **8**, 5056-5066.
154. L. Zhao, M. Tang, F. Wang and X. Qiu, *Fuel*, 2023, **331**, 125748.
155. S. A. Mahyoub, A. Hezam, F. A. Qaraah, K. Namratha, M. B. Nayan, Q. A. Drmosh, D. Ponnamma and K. Byrappa, *ACS Appl. Energy Mater.*, 2021, **4**, 3544-3554.
156. A. Primo, T. Marino, A. Corma, R. Molinari and H. García, *J. Am. Chem. Soc.*, 2011, **133**, 6930-6933.
157. A. Tanaka, K. Hashimoto and H. Kominami, *J. Am. Chem. Soc.*, 2012, **134**, 14526-14533.
158. N. Jiang, D. Li, L. Liang, Q. Xu, L. Shao, S.-B. Wang, A. Chen and J. Wang, *Nano Research*, 2020, **13**, 1354-1362.
159. S. Zhang, C. Chang, Z. Huang, Y. Ma, W. Gao, J. Li and Y. Qu, *ACS Catal.*, 2015, **5**, 6481-6488.
160. J. Rohlfs, K. W. Bossers, N. Meulendijks, F. Valega Mackenzie, M. Xu, M. A. Verheijen, P. Buskens and F. Sastre, *Catalysts*, 2022, **12**.